PCCP

Radiation effects on materials for electrochemical energy storage systems

Title: **Radiation effects on materials for electrochemical energy storage systems**

Tristan Olsen,[1, †] Cyrus Koroni,[1, †] Yuzi Liu,[2] Joshua A. Russell,[1] Janelle P. Wharry,[3,*] Hui Xiong[1,4*]

[1] Micron School of Materials Science & Engineering, Boise State University, Boise, Idaho, USA

[2] Center for Nanoscale Materials, Argonne National Laboratory, Lemont, IL, USA

[3] School of Materials Engineering, Purdue University, West Lafayette, Indiana, USA

[4] Center for Advanced Energy Studies, Idaho Falls, Idaho 83401, United States

† These authors contributed equally to this work

*Corresponding Author: clairexiong@boisestate.edu, jwharry@purdue.edu

ABSTRACT

Batteries and electrochemical capacitors (ECs) are of critical importance for applications such as electric vehicles, electric grids, and mobile devices. However, the performance of existing battery and EC technologies falls short of meeting the requirements of high energy/high power and long durability for increasing markets such as the automotive industry, aerospace, and grid-storage utilizing renewable energies. Therefore, improving energy storage materials performance metrics is imperative. In the past two decades, radiation has emerged as a new means to modify functionalities in energy storage materials. There exists a common misconception that radiation with energetic ions and electrons will always cause radiation damage to target materials, which might potentially prevent its applications in electrochemical energy storage systems. But in this review, we summarize recent progress in radiation effects on materials for electrochemical energy storage systems to show that radiation can have both beneficial and detrimental effects on various types of energy materials. Prior work suggests that fundamental understanding toward the energy loss mechanisms that govern the resulting microstructure, defect generation, interfacial properties, mechanical properties, and eventual electrochemical properties is critical. We discuss radiation effects in the following categories: 1) defect engineering, 2) interface engineering, 3) radiation-induced degradation, and 4) radiation-assisted synthesis. We analyze the significant trends and provide our perspectives and outlook on current research and future directions in research seeking to harness radiation as a method for enhancing the synthesis and performance of battery materials.

1. INTRODUCTION

Electrochemical energy storage (EES) systems such as batteries and electrochemical capacitors (ECs) are essential for a wide variety of applications ranging from personal electronics to electric vehicles (EVs). Moreover, beyond portable electronics and transportation applications, interest in developing large-scale EES systems in support of reliable, robust and cost-effective electrical power grids(1) using renewable energy sources, such as solar and wind—moving away from coal and fossil fuels—has been rising in the past few decades especially in recent years due to the pursuit of net-zero emissions to combat issues with climate change. The intermittent nature of the renewable energy sources(1–3) (e.g., wind and solar) entails the utilization of EESs such as rechargeable batteries for load leveling.(4) Furthermore, replacing gasoline-powered vehicles with EVs is an essential part of decarbonization strategies world-

wide.(5) However, existing electrochemical energy storage technology falls short of the performance requirements demanded by grid storage and electric vehicles. Research and development into making devices with higher efficiency, capacity, power, and stability are a critical need.(4,6) The main challenges facing existing EESs for such applications can be addressed by reducing their cost, increasing their lifespan, and reducing their size. These challenges are best addressed by increasing the energy/power density and stability of EESs, and therefore achieving reductions in size, materials, and cost.(5) Increasing demand for higher performing EESs is driven by the rapid growth of the EV market with a projected growth by 2030 of 15x the amount currently used today.(7) EVs, portable devices, robots, and rovers used for aerospace and space explorations depend on EESs with high energy/power density to perform. Some applications require EESs to operate outside of ideal conditions in extreme environments where exposure to radiation is a major concern. A growing area of research addresses the challenges facing EESs by studying the positive and negative effects of radiation (e.g., ion, electron, neutron, and gamma) on EESs materials.

To address how radiation in various forms affects the performance metrics of batteries and ECs, a brief overview of both is in order. While they operate on different working principles, both batteries and ECs include the same basic components: two electrodes, one positive (cathode) and one negative electrode (anode) at which electrochemical reactions take place, and a liquid or solid electrolyte that facilitates ion transport and impedes electron transport. Batteries tend to demonstrate an overall higher capacity with slower kinetics due to their reliance on faradaic reactions and bulk diffusion, whereas ECs have less capacity with faster kinetics due to surface processes for charge storage. The physiochemical properties of these devices are largely determined by the electrodes and electrolyte, and their interfaces. Tuning these properties for improved performance is a major goal for future development of high-performance EES. An important parameter that determines battery performance is the specific surface area of electrodes, and research related to increasing specific surface area using nanomaterials is an intense area of study.(6,8) Another exciting opportunity for improving battery and EC performance is the use of various types of radiation to modify the properties of battery materials.

Irradiation of materials lends itself to a number of different strategies for improving EES performance. One method of enhancing performance of electrodes is to intentionally introduce defects and disorder in electrode materials. Intentional introduction of defects – also known as defect engineering – in energy materials has conventionally been accomplished via doping and specific atmospheric exposure, and results in electrodes with enhanced electronic properties and electrochemical performance.(9–18) Ion irradiation is a novel approach to intentionally create defects in electrodes for batteries and ECs and therefore enhance their electrochemical performance.(19–22) This approach is advantageous because by controlling the energy of ions and ion dose, the extent and distribution of irradiation-induced defects can be tunably controlled. Additionally, the choice of ion species can be used to achieve n-type or p-type doping effects. Another way in which electrode performance can be improved by irradiation is via interfacial engineering. Interfacial modification of EES materials is accomplished by using irradiation to improve adhesion at interfacial regions, and mitigate undesirable cycling-induced stress.(23–25) Irradiation has also been utilized as a specific synthesis technique in various studies, and examples of this application will be discussed in a subsequent section.

Radiation-induced degradation of batteries and ECs is a major area of concern for applications in extreme environments such as nuclear reactors and aerospace.(26–31) An example of one such application is the 2011 Fukushima nuclear disaster, in which robots running on lithium-ion batteries were deployed in radiation intense environments.(32) High energy radiation (i.e., gamma and/or neutron) tends to have negative effects on EES performance, and frequently results in early failure of such devices. The long-term stability of EES is critical for practical applications, especially applications in which they are exposed to radiation. Thus, a better understanding of how radiation-induced degradations leads to premature failure will pave the way for designing more radiation tolerant devices, and methods for mitigating radiation damage.

In this review, we summarize the significant results of studies on the radiation effects of EES materials and discuss significant trends. The next sections will briefly describe the radiation effects of solids followed by review of recent work on four main areas: 1) defect engineering, 2) interface engineering, 3) degradation, and 4) synthesis. Finally, we will conclude by discussing future directions and the outlook for irradiated energy storage materials.

2. IRRADIATION EFFECTS

Irradiation refers to a process in which a target material is bombarded with energetic particles. These energetic particles generally transfer their kinetic energy to the target through either nuclear interactions or electronic interactions. Nuclear interactions are elastic collisions between particles and the nuclei of target atoms, whereas electronic interactions are inelastic collisions that consider the Coulombic and ionization effects between particles and the electron clouds of target atoms. The relative extent of nuclear versus electronic interactions is dependent upon the mass, charge, and energy of the incident irradiating particles, as well as the nature of the target material. This section will introduce these energy transfer mechanisms for several common irradiating particles, including neutrons, ions, electrons, and gamma rays (i.e., photons).

2.1. Neutron Irradiation

Neutron irradiation effects are the result of atomic displacement occurring from the bombardment of moderately energetic (i.e., ~10s eV to 20 MeV) neutrons onto a target, which primarily originate from fission reactions. In practice, neutron irradiations are conducted in nuclear fission reactors or neutron generators. The radiation damage occurs through elastic scattering interactions between the incoming neutrons and the nuclei of atoms in the target sample, displacing atoms from their equilibrium lattice positions. These atomic displacements occur when the value of the energy transferred from the neutron to the atom during the elastic collision exceeds the atomic displacement energy (E_d). The maximum value of the transferred energy, denoted by $\hat{T}$, is directly proportional to the neutron energy (E) and inversely proportional to the atomic mass (M) in units of amu (33):

$$\hat{T} = \frac{4ME}{(M+1)^2} \#Eq. 1$$

Following the elastic energy transfer from the neutron to the atom, the displaced atom becomes a fast-moving primary knock-on atom (PKA), with kinetic energy defined by the difference between $\hat{T}$ and E_d. A domino-like effect can subsequently occur in the target material, in which the PKA can proceed to undergo elastic interactions with other atoms in the lattice. This process creates further atomic displacements, leaving behind vacancies in their original lattice positions, until the energy of the displaced atoms falls below the value of $2E_d$, at which point the displaced atom comes to rest (kinetically) as an interstitial. These successive collisions are defined as a displacement cascade, and are shown in Figure 1, which also illustrates unique crystallographic phenomena such as channeling and focusing.(34)
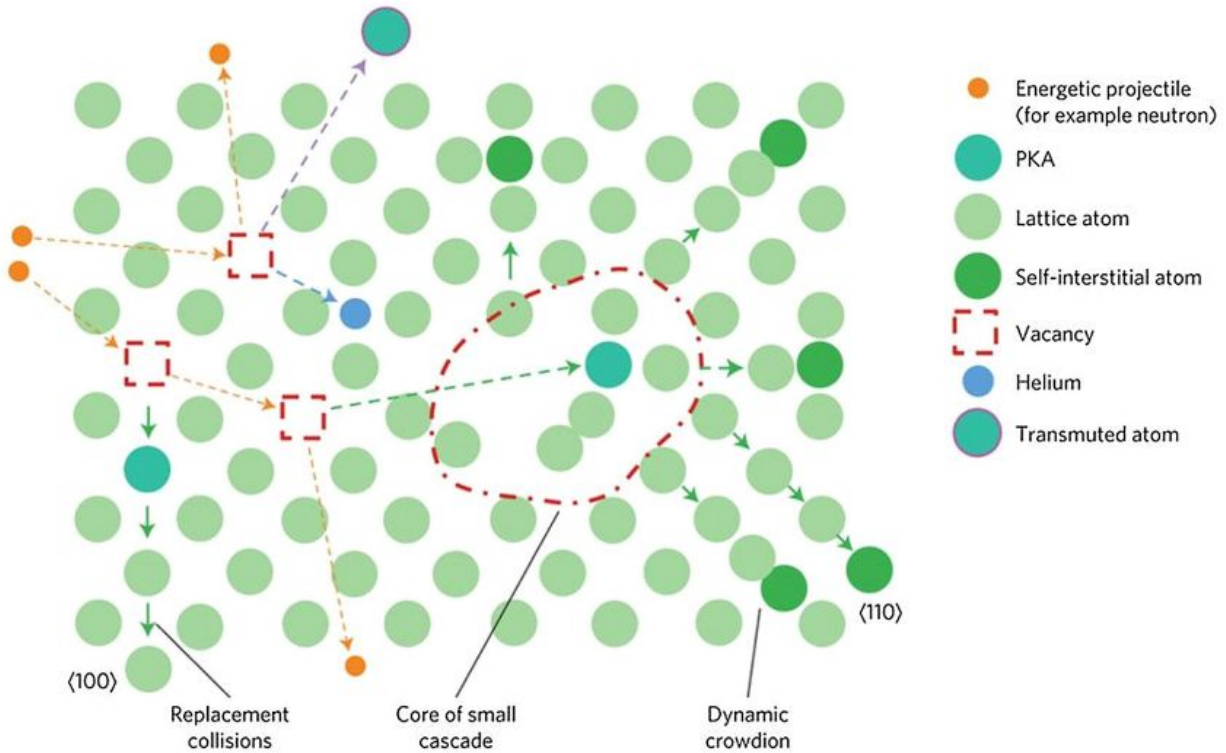
Figure 1. *Schematic of neutron irradiation damage. Reproduced from Ref. (34) with permission from Springer Nature, copyright 2019 .*

2.2. Ion Irradiation

Ion irradiation of materials involves the transfer of kinetic energy from the incident ion to the target atoms through collisions with both electrons and nuclei. These interactions collectively result in the incident ion transferring its kinetic energy to the target material through three major contributions which can be seen in Equation 2(35):

$$S(E) = -\frac{\delta E}{\delta x} = -\left(\frac{\delta E}{\delta x}\right)_{nucl.} - \left(\frac{\delta E}{\delta x}\right)_{elec.} - \left(\frac{\delta E}{\delta x}\right)_{rad.} \#Eq.\,2$$

Where $\frac{\delta E}{\delta x}$ is the differential energy loss per unit distance of travel, and is the sum of the contributions of nuclear, electronic, and radiative energy losses. The radiative term is generally negligible for ion energies in the ~eV-GeV range. Over this range of energies, the relative magnitudes of the nuclear and electronic energy losses vary.(36) Nuclear stopping is the dominant energy loss mode at lower incident ion energies, whereas electronic stopping is the dominant energy loss mode at higher incident ion energies. At intermediate energies, both nuclear and electronic stopping occur, leading to a complex combination of both energy loss mechanisms in the irradiated sample.(35,37–40)

Nuclear stopping can be described by the binary collision approximation (BCA) model in which the incident ion undergoes a sequence of independent elastic collisions with target atoms; between elastic collisions, the ion is assumed to travel in a straight path.(41) If the elastic collisions result in a transfer of energy from the incident ion to the target atom of $>E_d$, a Frenkel pair will form from the displaced atom and the vacancy left behind in its original lattice position.(41) Like with neutron irradiation, displaced

atoms with sufficient energy may subsequently collide with additional atoms within the lattice, leading to a collision cascade. Electronic stopping, on the other hand, describes energy losses from the incident ion through inelastic ionization collisions with the electrons of the target atoms. These effects are often described by the thermal spike model, where electrons along the path of the incident ion become excited due to the transfer of energy through electron-phonon coupling and local heating.(42,43) Electronic stopping often produces ion tracks within the target material; along these tracks, amorphization and/or crystallization may occur, and point defects can also be generated.

2.3. Electron Irradiation

Energetic incident electrons can interact with the nuclei or the electronic subsystem in target atoms. Atomic displacements are uncommon because of the extremely low electron mass relative to that of a nucleus. In other words, electrons must have extremely high kinetic energy in order to transfer enough energy to a nucleus to induce a displacement. However, electron-electron interactions are possible, regardless of the incident electron energies, causing ionization or bond breakage. These interactions also do not typically result in atomic displacements, although chemical reactions may occur (44), leading to altered material properties and performance.

2.4. Gamma Ray Irradiation

Gamma rays – or photons – primarily interact with the electrons of a target material through photoelectric absorption, Compton scattering, or pair production(45). Photoelectric absorption occurs when the gamma ray loses all of its energy to a bound electron, typically a more tightly bound electron. This energy is absorbed by the electron, some of which is used to overcome the electronic binding energy and the rest is transferred as kinetic energy to the freed electron. A small amount of energy remains through momentum conservation laws and becomes recoil energy of the atom. When the gamma ray only transfers some of its energy to a loosely bound or freed electron, the interaction is called Compton scattering. If the interacting electron is bound, it becomes a free electron with kinetic energy equal to the difference of the energy lost by the gamma ray and the electron binding energy. Both the electron and the scattered gamma ray leave the interaction site. Lastly, pair production occurs when a gamma ray with an energy of at least 1.022 MeV creates an electron-positron pair when under the influence of a strong electromagnetic field in the vicinity of an atomic nucleus. Energies higher than 1.022 MeV become split evenly among the electron and positron as kinetic energy. Following loss of their kinetic energy, the electron and positron recombine in an annihilation process that subsequently creates two gamma rays of equal and lesser energy than the incident gamma ray. These gamma rays may then proceed to excite other electrons through photoelectric absorption or Compton scattering interactions.

2.5. Other Irradiation Treatments

Plasma-jet irradiation, also known as atmospheric pressure plasma jet (APPJ), is a phenomenon in which cold plasmas are generated at atmospheric pressure using rare gases such as helium or argon(46). APPJ is generated by an excitation typically through either alternating current (AC) voltage or direct current (DC) voltage. The generated plasma contains numerous charged particles, ionized gas species, free radicals, and other complex reactive species. APPJ can achieve surface modification of target materials in a short period of time through highly reactive particles hitting the target surface(47).

Microwave irradiation is comprised of electromagnetic radiation in the frequency range of 300 MHz to 300 GHz, and causes charged or polar particles to tend to align themselves with the electric field component of the microwaves(48). If the particles fail to align themselves as quickly as the direction of the electric field of microwaves changes, friction is created which introduces heat in the target material. Localized hotspots can have elevated temperatures of 100-200K higher than the bulk material. This increased temperature can lead to chemical reactions within the target material.

3. IRRADIATION OF ENERGY MATERIALS

All of the aforementioned irradiation types have been reported to alter the performance of various energy materials through intentional introduction of defects (i.e., defect engineering), creation or tailoring of interfaces (i.e., interface engineering), or introduction of damage and degradation. Irradiation has also been employed to assist in the synthesis of energy materials. This section will review the scientific literature on irradiation of energy materials. The section is organized into four sub-sections – defect engineering, interface engineering, degradation, and synthesis – and some sub-sections are further subdivided into materials for batteries and capacitors. All literature reviewed in these sub-sections are summarized in Table 1.

3.1. Defect Engineering

The goal of defect engineering in battery materials is generally to enhance the electrochemical properties of positive or negative electrode materials through introduction of defects and control of defects (e.g., size control of grain boundaries and nanocrystalline regions). Generation of point defects – such as vacancies, and interstitials – have been shown to improve the capacity, charge transport kinetics, and cycling performance of battery electrodes.(9–11) These enhancements to battery performance are accomplished by increasing intercalation sites, electrical conductivity through doping, and facilitated charge transport due to the presence of vacancies. A growing area of research utilizes ion irradiation as a method for intentionally creating defects in electrode materials in order to enhance electrochemical performance.(19–21,49,50) For electrochemical capacitors, charge storage is associated with surface phenomena (e.g., electrical double layer, pseudocapacitive processes), whereas batteries involve both surface and bulk interactions. But similar to batteries, electrochemical charge storage in capacitors can be enhanced through the formation of point defects.(17,49) Capacitors are also particularly sensitive to edge defects and edge sites due to the primary role the surface plays in influencing the charge storage properties of capacitors.(49,50) It has also been shown that accumulation of point defects in some materials can facilitate high electronic conductivity while also enabling heat conduction.(18) This section summarizes literature that has demonstrated enhanced electrochemical performance due to intentional introduction of irradiation defects.

3.1.1. Materials for Batteries

Electrode Materials for Lithium-Ion Batteries - Some studies have demonstrated that ion irradiation of negative electrode materials can enhance their electrochemical performance. For example, Smith et al. have shown that proton irradiation of both amorphous and anatase TiO_2 nanotube electrodes can yield measurable improvements in battery performance metrics as a result of microstructural changes, irradiation induced phase transformations, and defect accumulation.(19–21) An important consideration for ion irradiation of materials for batteries is the inherent depth dependence of the technique, and how that relates to nuclear and electronic stopping power. In Smith and coworkers' study of ion irradiation of 3 MeV Nb^+ ions in (100) oriented rutile single crystal TiO_2, it was found that post irradiation microstructure has a strong dependence on nuclear and electronic stopping power, and that this has further ramifications for Li insertion into the material. In Figure 2a, cross-sectional transmission electron microscopy (TEM) shows that 3 MeV Nb^+ implantation of the material results in four distinct damage regions ranging from the surface to a depth of about 1700 nm. The first region extends to ~60 nm from the surface, and shows short-range disordering along with long-range reorientation due to ion channeling effects. The second region has microstructure that is largely governed by nuclear stopping, exhibiting irradiation-induced dislocation loops that are parallel to the ion beam direction, which appear as darkly contrasting regions that are adjacent to lighter contrasting highly ordered rutile regions. The third region is largely governed by electronic stopping power and is characterized by the appearance of dislocation

loops that are perpendicular to the ion beam direction. The fourth region corresponds to the peak Nb^+ implantation region, at which the Nb ions have lost most of their energy, and the change in contrast is primarily due to nanoscale atomic rearrangements from Nb implantation, while long-range ordering is retained. Subsequently, the Nb irradiated sample was lithiated to simulate the effects that Li intercalation might have on the material if it were used as a negative electrode in a LIB. The resulting energy-filtered TEM (EFTEM) map shows that Li concentrations are highest in the second and fourth regions, which correspond to the areas with the highest concentration of dislocation loops and the peak Nb implantation zone, respectively (Figure 2b).
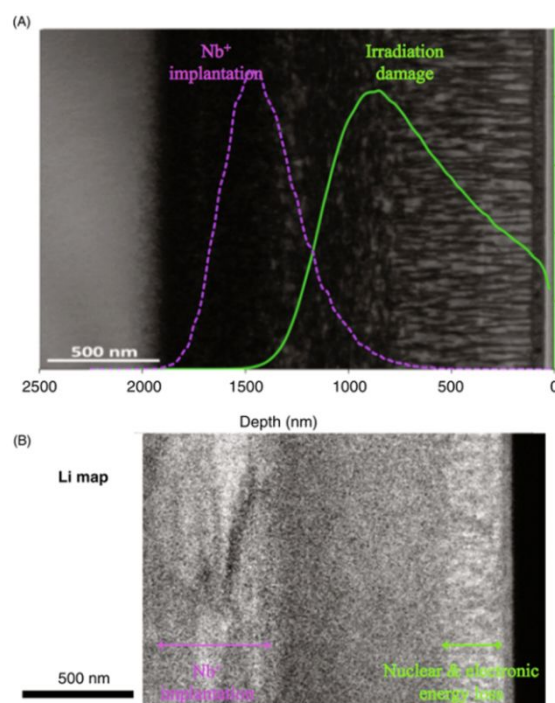
**Figure 2.** *(a) Cross-sectional TEM showing the four-layered defect structure of 3 MeV Nb^+ irradiated single crystal rutile TiO_2, and (b) EFTEM map showing Li concentration (in light contrast) with corresponding Nb implantation and damage peaks. Reproduced from Ref. (21) with permission from the American Ceramic Society, copyright 2018, and Ref. (22) with permission from Elsevier, copyright 2022.*
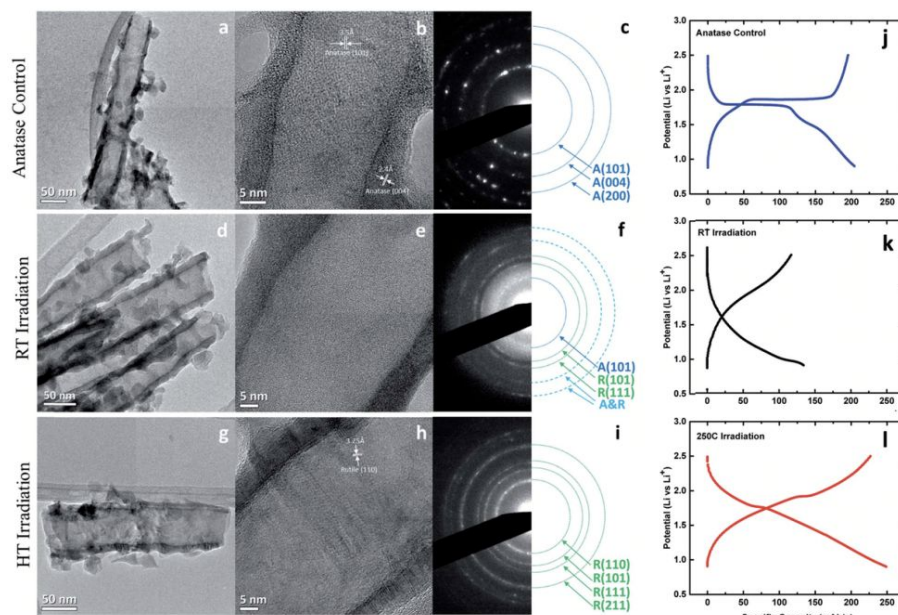
Figure 3. *(a, d, g) Low magnification TEM images of unirradiated TiO$_2$ anatase nanotubes, 20ºC irradiated amorphous TiO$_2$ nanotubes ("RT"), and 250ºC irradiated amorphous TiO$_2$ nanotubes ("HT"), respectively; (b, e, h) HRTEM images of unirradiated, RT irradiated, and HT irradiated nanotubes and their corresponding selected area diffraction (SAED) patterns; (c, f, i) indexing of the SAED patterns, with A indicating anatase and R indicating rutile; (j, k, l) charge/discharge profiles of unirradiated anatase, RT irradiated, and HT irradiated nanotube anodes. Reproduced from Ref.(20) with permission from the Royal Society of Chemistry, copyright 2017.*

Proton irradiation effects on amorphous TiO$_2$ nanotube negative electrodes were investigated by Smith et al.(20). TiO$_2$ nanotubes were prepared via electrochemical anodization on titanium foil and were grown to a length of approximately 1 μm. The amorphous samples were irradiated with protons at 200 keV to a dose of 0.17 displacements per atom (dpa), corresponding to a total fluence of 2.18×10^{17} ions/cm^2 at either room temperature (RT) or 250ºC (high temperature - HT).(20) Proton irradiation resulted in an amorphous-to-crystalline transformation that was temperature dependent: irradiation at RT resulted in the formation of a mixture of anatase and rutile TiO$_2$, while the HT irradiation yielded a disordered rutile phase (Figure 3c, 3f, and 3i). From galvanostatic cycling in Li-metal half cells, it was found that the HT irradiated TiO$_2$ nanotubes had enhanced capacity (~250 mAh/g) when compared to an anatase control (~200 mAh/g). However, the RT irradiated TiO$_2$ nanotubes had the lowest capacity of the three at about 130 mAh/g. The voltage profile for the anatase control shows a plateau region that is consistent with Li insertion via a two-phase process (Figure 3j). Both irradiated samples have sloping curves that are indicative of a single-phase solid solution behavior (Figure 3k, l).(20) The enhanced capacity of the HT irradiated sample was attributed to the irradiation-induced formation of a disordered rutile phase with increased storage sites due to irradiated-induced defects, while the relatively poorer performance of the mixed anatase/amorphous/rutile phase for the RT sample was attributed primarily to interference from the different phases impeding Li diffusion in the sample.
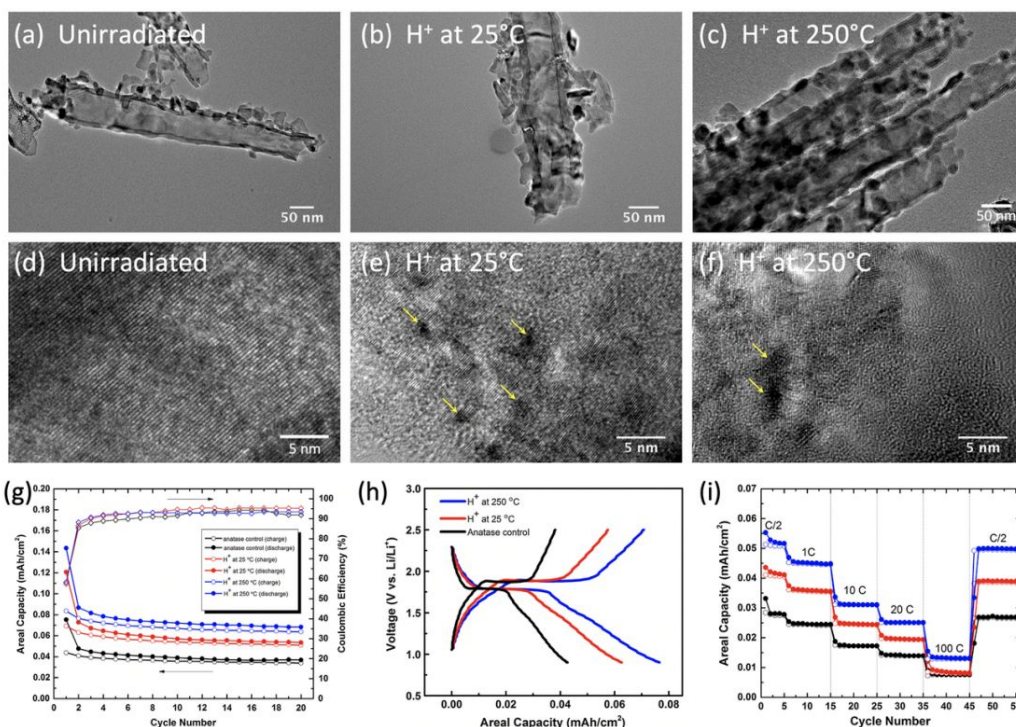
Figure 4. *(a-c) Low magnification images of anatase nanotubes in the unirradiated, proton irradiated at 20°C ("RT"), and proton irradiated at 250°C ("HT") conditions, respectively; (d-f) HRTEM images of unirradiated, RT, and HT irradiated anatase nanotubes; (g-i) electrochemical characterization data showing areal capacity, charge/discharge profiles, and rate capability of anatase control (black), RT irradiated (red), and HT irradiated anatase nanotubes (blue). Reproduced from ref.* (19) *with permission from Springer Nature, copyright 2019.*

In a similar study, irradiation of anatase TiO_2 nanotubes at RT and HT with protons was found to have positive effects on electrochemical performance.(19) TEM analysis (Figure 4a-c) suggests that nanotube morphology was not significantly changed by proton irradiation, but HRTEM analysis shows that evidence of defect clusters forming after proton irradiation (darkened regions indicated by yellow arrows, Figure 4e-f). It was also observed that the defect clusters were larger and more abundant after HT irradiation than RT irradiation. From the electrochemical characterization (Figure 4g-i), areal capacity and rate capability increased as a result of proton irradiation at both RT and HT, and HT irradiated nanotubes exhibiting the highest areal capacity and rate capability. This improvement in electrochemical properties was largely attributed to enhanced Li intercalation due to accumulated defects induced by proton irradiation. Additionally, electrochemical impedance spectroscopy (EIS) analysis of the samples indicated that both RT and HT irradiated samples had higher Li diffusivity than the unirradiated anatase control.

The effects of ion implantation on the surface of graphite were investigated by Hai et al. with 50 keV N^+ and C^+ at a fluence of 1 x 10^{12} ions/cm² for both species(51). Stopping and Range of Ions in Matter (SRIM) was used to illustrate the depth of the ion irradiation which was around 50-160 nm for both N^+ and C^+. Raman spectroscopy revealed the effects of irradiation by monitoring the D-band and G-band which correspond to structural defects within the graphite and the in-plane symmetric stretching of graphitic sp² carbons, respectively. The graphite irradiated with nitrogen (GCN) showed increased intensities for both bands as well as broadened peak width. The peak intensity ratio (I_D/I_G) for the unirradiated graphite (GC) and GCN were 0.29 and 0.42, respectively, indicating that the degree of graphitization decreases following nitrogen implantation. The graphite irradiated with carbon (GCC) had I_D/I_G ratio of 0.36 showing that although it had a higher degree of graphitization than GCN, the defects

were still greater than in GC. An additional annealed sample of GCN showed an I_D/I_G ratio of 0.3, suggesting partial recovery of irradiation defect through annealing. X-ray photoelectron spectroscopy (XPS) analysis of the GCN sample suggests the existence of pyridinic and pyrrolic nitrogen, which is a result of N^+ becoming incorporated into the C-C bonds of graphite. Cycling stability studies for GC and GCN were conducted over 100 cycles, showing the initial capacities at 537 and 725 mAh/cm³, respectively. Following 100 cycles, GCN had a decrease in capacity to 708.7 mAh/cm³ which was still higher than GC. This improvement was a result of the existence of vacancies and layer damage of the graphite which provide accommodation and transportation channels to allow for Li^+ intercalation. Utilizing EIS analysis, GCN showed improved electronic conductivity and decreased charge-transfer resistance as compared to GC. The diffusion coefficient for GCN was also higher than that for GC. The authors stated that the N^+ irradiation improved the wettability of the electrolyte and the electronic conductivity of the graphite electrode while also providing vacancies for higher Li^+ diffusion. They also investigated the effect of nitrogen dopant and vacancies by comparisons to the GCC and annealed GCN samples, and suggested that the effect of the nitrogen dopant is more important than vacancies on the surface.

The effects of Cu ion implantation on the cycling stability of Si negative electrodes for LIBs has been investigated by Hu et al.(52) They studied 60 nm Si films on Cu foil that were implanted with 95 keV Cu ions to a fluence of 7.5×10^{16} ions/cm². Unirradiated Si film exhibited significant fractures on the surface after 100 cycles. But by contrast, Cu irradiated films remained similar in appearance and did not exhibit significant cracking even after 100 cycles. Additionally, when the cross-sections of samples before and after lithiation were compared under scanning electron microscopy (SEM), a 188% increase in volume was observed for the unirradiated Si film as compared to a volume increase of 49% in the irradiated sample. From the cycling results, it was found that the initial charge capacity of the unirradiated Si film was higher than the Cu irradiated film – 2308 mAh/g versus 807 mAh/g (Figure 5a, c). However, the capacity of the unirradiated Si sample began to fade rapidly after about 20 cycles, and stabilized to 224 mAh/g after ~200 cycles (Figure 5b). The Cu irradiated Si sample exhibited enhanced cycling stability, with about 84% of the original capacity retained after 300 cycles (Figure 5d). The authors ascribed the improved cycling performance of the irradiated Si film to the formation of Cu and Cu/Si alloy (Cu_3Si) nanoparticles in the Si film to stabilize the structure and mitigate stress from volume change during cycling(52).
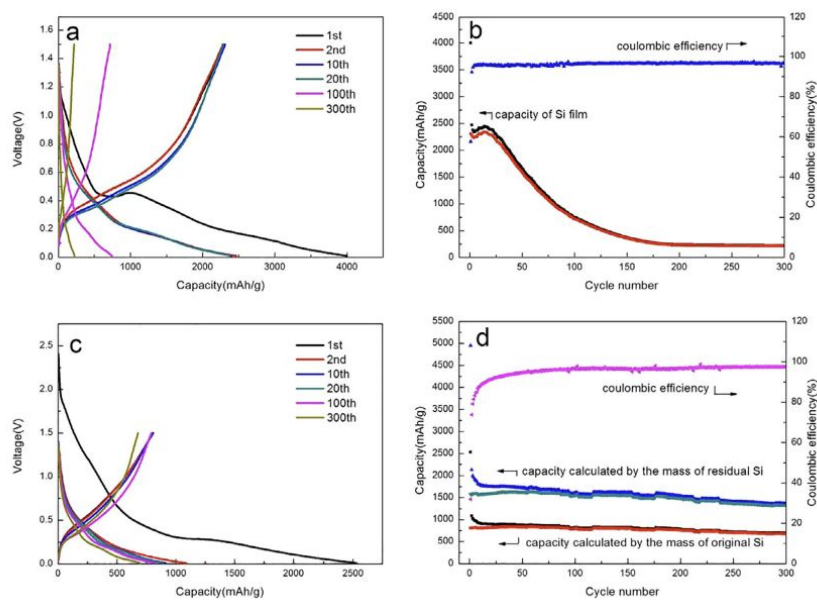
Figure 5. *(a) Charge/discharge curves carried out at a rate of 1000 mA/g for unirradiated Si and (b)*

cycling performance of unirradiated Si over 300 cycles; (c) charge/discharge curves for Si irradiated with Cu ions and (d) cycling performance of irradiated Si. Reproduced from ref. (52) with permission from Elsevier, copyright 2019.

A study completed by Kozlovskiy et al. looked at 68 MeV Ca^{5+} irradiation on Ni nanotubes with irradiation fluences of $1 \times 10^{10} - 1 \times 10^{11}$ ions/cm^2 to identify the structural characteristics as well as the directional modification of the nanotubes in LIBs(53). X-ray diffraction (XRD) revealed that at a fluence of 1×10^{11} ions/cm^2 there was a change in the texture orientation seen in the (220) direction. They suggested that this reorientation of crystallites in the (220) direction may be due to the active migration of the formed defects to the sinks at the grain boundaries, followed by recrystallization and a change in their orientation in that direction. Additionally, as irradiation fluence increased, there was a decrease in distortions in the crystal lattice which is indicative of a decrease in deformations in the lattice. The irradiated samples displayed increased crystallinity, suggesting that irradiation may be a useful tool to improve structural characteristics without changing the structural integrity or phase composition of the nanotubes. Electrochemical results showed that the cycle life of the cells made from the irradiated specimen were extended by 1.5 times over the unirradiated control. When cells were limited in their maximum charge capacity at 1000 mAh/g, the unirradiated samples performed well up to ~350 cycles, but following irradiation these cells were able to reach >555 cycles. Similar results were also found at higher maximum charge capacities of 1500 and 2000 mAh/g. The extended lifetimes of the cells were due to the partial ordering of the crystal structure from irradiation; additional boundaries created during irradiation impeded the process of degradation by annihilating the defects and allowing for dense packing of crystallites.

The effects of W and Mo ion implantation-induced defects on the electrochemical energy storage properties of MoS_2 electrode materials have been investigated by Mwonga et al.(54) Irradiations were completed at an energy of 10 keV with fluences of 1×10^{14} ("Mo-14"), 1×10^{16} ("Mo-16"), and 2×10^{16} ("Mo-2e16") ions/cm^2 for Mo ions and at fluences of 1×10^{12} ("W-12"), 1×10^{14} ("W-14"), and 1×10^{16} ("W-16") ions/cm^2 for W ions. Raman spectroscopy revealed an irradiation-induced decrease in two peaks at 383 and 408 cm^{-1} associated with vibrations in-plane from two S atoms with respect to Mo atom E^1_{2g} and out-of-plane A_{1g} of only S atoms, respectively. There was no obvious trend amongst the specimens in regard to the degree or extent of peak disappearance. CV analysis showed that the peak-to-peak separation of the anodic and cathodic reactions (ΔE_{pp}) was smallest for the pristine and W-14 samples. The smaller the ΔE_{pp}, the faster the kinetics, which is conducive to enhanced rate capability and power performance. Additionally, the area under the reduction curve in CV represents the amount of energy stored by the sample, and it can be seen that the W-12 and Mo-16 give the highest values. The authors suggested that the higher charge storage for W-12 may be attributed to the increased damage to the surface of the electrode providing more surface area for charge storage. They also provided an alternative explanation that the high charge storage seen for W-12 may also be due to implanted W atoms that are in between the layers of MoS_2 providing the material more support for intercalation of Na ions. Also the *b*-values extracted from CV ranged from 0.18 to 0.61 showing that the electrodes undergo diffusion-controlled processes more similar to batteries than electrical double layer capacitor (EDLC). Note that 0.18 for a *b* value is unreasonable as *b* cannot be smaller than 0.5 so the analysis done is questionable. The diffusivities were also highest for W-12 and Mo-16 samples at ~8 x 10^{-4} cm^2/s. The authors suggest that the resistance to the Na-ion transport found in the samples W-12 and Mo-16 was lower than in other samples. The Mo-2e16, Mo-14, and W-12 showed the highest discharge specific capacity values of ~2.35, ~1.75, and ~2.35 µAh/cm^2.

Rahman and coworkers investigated the effects of 1 MeV Kr ion irradiation on $Na_{2/3}Fe_{1/2}Mn_{1/2}O_2$ to a total fluence of 6.25×10^{14} ions/cm^2, and $LiNiO_2$ layered cathode materials to a total fluence of 1.25×10^{15} ions/cm^2, via *in situ* TEM.(55) Irradiation was performed at -173, 20, and 200 °C. They found that $LiNiO_2$ was more resistant to irradiation-induced structural changes and amorphization than $Na_{2/3}Fe_{1/2}Mn_{1/2}O_2$, possibly due to Li^+ and Ni^{3+} ions having similar radii, which lowers the energy

required to form cationic antisite defects. The difference between ionic radius for Na^+ and $Fe^{3+}/Mn^{3+}/Mn^{4+}$ cations for the Na-layered material is more significant, which leads to higher energy requirements for cation antisite defects, and therefore lower resistance to irradiation-induced structural changes. Their results were also consistent with the theory that elevated temperatures should enhance radiation resistance of crystalline materials due to annihilation of irradiation-induced defects occurring more frequently.

In an example of plasma jet irradiation being used to modify electrodes, Lin et al. investigated the effects of Ar/N_2 plasma on the electrochemical performance of lithium titanate, $Li_4Ti_5O_{12}$ (LTO) carbon containing laminated electrodes for LIBs.[47] Irradiation was performed on LTO electrodes containing conductive carbon and using a Ar/N_2 beam with a power of 100W for 30, 45, and 60 s. Characterization via optical emission spectroscopy and XPS confirmed that Ar/N_2 plasma bombardment produced C-N and N_2 bonding was present in the carbon/LTO matrix. The electrochemical results show that plasma jet irradiation led to enhanced rate capability compared to the unirradiated control, with the 30 s exposure being the most improved. Additionally, the LTO electrode irradiated for 45 s had superior cycling performance at both 1C and 10C rates, while exhibiting lower capacity fade and higher specific capacity. At 1C, the 45 s irradiated electrode had a specific capacity of ~150 mAh/g after 50 cycles, while the unirradiated control had a specific capacity of ~110 mAh/g. At 10C, the values were ~115 mAh/g and ~40 mAh/g for the 45 s irradiated sample and unirradiated sample, respectively. Analysis via EIS also showed that the 45 s irradiated LTO electrode had higher electrical conductivity and enhanced Li diffusivity compared to the unirradiated control. This improvement in performance was largely attributed to plasma jet irradiation effectively N doping the carbon/LTO electrodes, and improvement of the carbon conducting network by the same.

Electrolyte Materials for Solid-State Batteries - Ion implantation was utilized in a solid-state electrolyte (SSE) of $Li_{6.4}La_3Zr_{1.4}Ta_{0.6}O_{12}$ (LLZTO) to create compressive stress for use in SSE batteries by Yao et al.[56]. Samples of LLZTO were irradiated using a combination of 190, 150, 80, and 50 keV Xe ions to create a flat damage profile and uniform distribution of Xe as a function of depth into the specimen. Samples were denoted depending on the total fluence as LLZTO-L (1 x 10^{12} ions/cm^2), LLZTO-M (1 x 10^{13} ions/cm^2), and LLZTO-H (1 x 10^{14} ions/cm^2). To understand the effect of stress on the SSEs and the changes that occur in the lattice, molecular dynamics (MD) simulations were performed. LLZTO was simulated at 300 K under different levels of stress (tensile stress of 10 GPa and compressive stress of -10, -20, and -30 GPa). A compressive stress slightly lowered Li^+ diffusion, whereas increasing tensile stress increased Li^+ diffusion. The changes in the lattice parameters as a result of stress showed that the lattice volume increased under tensile stress; there is a corresponding increase of Li diffusion in the system from 9.24×10^{-5} to 3.89×10^{-4} Å/ps when the tensile stress is increased from 0 to 10 GPa. The authors point out that although the compressive stress does not contribute to increasing Li^+ diffusion, its benefit is in forcing cracks generated by the Li dendrite formation to close. Compressive stress present in SSEs could contribute to inhibiting the propagation and penetration of dendrites. Experimentally, the authors made symmetrical cells with Li and LLZTO. The cell electrochemical performance was evaluated by Li plating/stripping with a current density of 0.1 mA/cm^2. The LLZTO pellets showed a drop of potential following 20 hrs with the cells behaving like a short-circuit state with its potential close to 0 V. The LLZTO-L cells similarly exhibited a potential drop around 20 hrs, though they demonstrated higher potential values that fluctuated differing them from LLZTO pellet cells. For LLZTO-M and LLZTO-H with higher amounts of irradiation, they both demonstrated improved performance: LLZTO-M showed 300 hrs with no drops in potential during the cycling, while LLZTO-H also had no drop in potential although around 40 cycles the potential began to increase. The authors concluded that the LLZTO and LLZTO-L had similar degradation behavior of short-circuit after 20 hrs, LLZTO-H showed extended :o stripping/plating but had an increase in impedance, and lastly that LLZTO-M samples had the capability to extend the battery life without a short-circuit. The authors used Raman spectroscopy and grazing incidence XRD (GI-XRD) to study the crystallinity of the samples and showed that with higher

irradiation doses there was lower crystallinity, which may explain the improved lifespan of LLZTO-M and LLZTO-H samples. The increased atomic displacements also correspond to increased compressive stress at the surface of the LLZTO-M and LLZTO-H samples. However, with increased irradiation, defect clusters may be lost to the surface, which in turn could lead to disconnected crystalline regions and higher impedance as seen through the loss of structural integrity in the LLZTO-H sample. The authors conclude that the LTZTO-M – with a Xe fluence of 1 x 10^{13} ions/cm^2 – exhibited the most enhanced durability to Li plating and stripping, and that this technique provides a route towards engineering SSEs that are better at suppressing Li dendrite growth.

In a more fundamental study, electron irradiation has been used to study how irradiation-induced defects initiate phase transformations in candidate cathode materials, and show how specific defects facilitate Li or Mg intercalation during electrochemical cycling.[57,58] Wei et al. studied the effects of electron irradiation on metastable states of Li_2FeSiO_4 and $LiFePO_4$ via *in situ* TEM. Both materials undergo a dose dependent transformation to amorphous then crystalline phase as a result of electron irradiation. Li_2FeSiO_4 transformed at lower fluences than $LiFePO_4$ and the transformation in both materials seemed to depend on a threshold dose.[58] Okamoto et al. found via *in situ* TEM measurements that spinel $MgCo_2O_4$ readily transforms to a defect rocksalt structure with cation disorder.[57] This process is facilitated by cation migration from tetrahedral sites to adjacent octahedral sites. A similar transformation from spinel to rocksalt occurs due to Mg ion insertion, which confirms the feasibility of $MgCo_2O_4$ as a candidate material for intercalation of Mg ions in Mg-metal anode batteries. An additional study on the electron irradiation effects of $Li_4Ti_5O_{12}$ (LTO) showed that its electronic conductivity may be improved up to 5 orders of magnitude while maintaining the good Li conductivity[59]. Exposure to electrons in a scanning TEM (STEM) transformed the LTO from a spinel to a rocksalt structure that could be organized into nanochannels within the anode material, which demonstrated improved electrical conductivity.

Finally, the effects of Ar/N binary plasma jet irradiation on LTO electrodes for battery performance was reported[60]. LTO was exposed to the plasma for 1 min at a power of 300 W. The plasma irradiated LTO ("P-LTO") samples showed Ti reduction from Ti^{4+} to Ti^{3+} as well as nitrogen in the N^{3-} oxidation state occupying and replacing the O^{2-} vacancies that formed during irradiation. SEM imaging conducted in both secondary electron mode (Fig. 6a-6b) and backscattered electron mode (Fig. 6c-6d) showed that plasma jet irradiation resulted in a reduction of LTO particle size. Rate performance data was evaluated at 0.5C, 1C, 5C, 10C, and 1C between the LTO and P-LTO showing improved rate performance of the P-LTO sample (Figure 6e). Cycle stability was also dramatically improved when plasma irradiated at rates of 1C, 5C, and 10C. These enhancements were attributed by the authors to improved Li diffusion rates as a result of the N doping into the O vacancy sites and the partial reduction of the Ti. EIS was applied to understand the kinetic behavior and it was found that the charge transfer resistance of the P-LTO was lower than that of the pristine LTO. The semicircle diameter in the high frequency range was significantly smaller for the P-LTO sample than for the LTO. The authors suggested that the smaller charge transfer resistance of the P-LTO also reflected the higher electrical and Li conductivity of the bulk LTO improved by plasma irradiation. Additionally, the calculated diffusion coefficient of the P-LTO was much higher than that of LTO showing improved electrochemical kinetic performance following plasma irradiation. The authors conclude that the observed improvements in Li diffusion and electrochemical performance can be ascribed to the formation of oxygen vacancies in the P-LTO, and doping of N^{3-} into oxygen lattice sites.
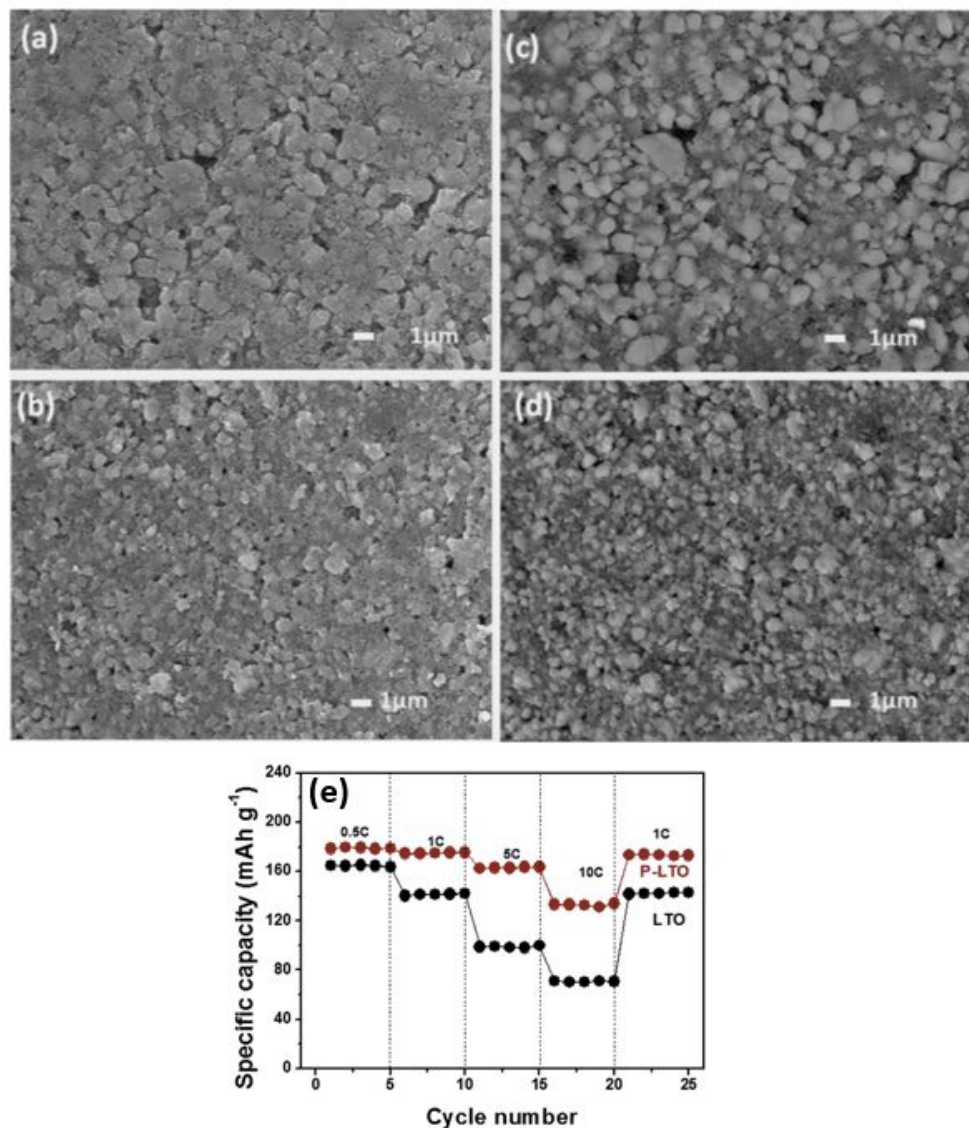
Figure 6. *LTO (a) before and (b) after plasma irradiation, shown in secondary electron imaging mode; and (c) before and (d) after plasma irradiation, shown in backscattered electron imaging mode, with the corresponding (e) rate performance of irradiated ("P-LTO") and unirradiated ("LTO") materials. Reproduced from Ref. (60) with permission from Elsevier, copyright 2015.*

3.1.2. Electrochemical Capacitors

The effect of Ag ion irradiation was studied at 60 keV and fluences ranging 0.5 x 10^{17} – 1.0 x 10^{18} ions/cm^2 on anodically grown TiO_2 nanotube negative electrodes for capacitors.(61) The surface morphology of the TiO_2 nanotubes changed significantly as a result of irradiation. At lower irradiation fluences (0.5 x 10^{17} and 1 x 10^{17} ions/cm^2), a surface film layer formed while the underlying tube structure appeared to be unaffected. At higher fluences (5 x 10^{17} and 1 x 10^{18} ions/cm^2), both the surface and the underlying tube structure were significantly affected, and the overall tube structure was reduced in length and had rougher side-walls compared to the unirradiated control. These irradiation-induced morphological changes were attributed to the combined action of local heating from the ion beam, and

damage and disordering caused by ion bombardment. Capacitance and resistivity of the samples was measured in a three-electrode cell with 0.5 M Na_2SO_4 solution and a standard Calomel reference electrode. Resistivity decreased with increasing Ag ion fluences of 0.5, 1, and 5 x 10^{17} ions/cm², with the minimum resistivity being 21.6 Ω-cm at 5 x 10^{17} ions/cm² – a reduction of 95.8% in resistivity compared to the unirradiated control (523.7 Ω-cm). However, at 1 x 10^{18} ions/cm², the resistivity increased to ~200 Ω-cm, indicating that irradiation-induced changes at this highest fluence had a negative impact on conductivity. Volumetric capacity was greatly enhanced by Ag ion implantation with the highest capacity (9324.6 mF/cm³) occurring at fluence of 5 x 10^{17} ions/cm². However, it was also found that the capacity dropped to nearly the same value as the unirradiated sample (32.9 mF/cm³) at a fluence of 1 x 10^{18} ions/cm³ (54.3 mF/cm³).

Le Calvez et al. investigated the influence of As ion irradiation on the pseudocapacitive behavior of vanadium nitride (VN) thin films at energies between 20-150 keV to a constant fluence of 1 x 10^{15} ions/cm².(62) TEM imaging showed that the as-prepared VN films had a columnar microstructure with intercolumnar porosity (Figure 7a). Maximum implantation depth was calculated for As ions at various energies, and it was found that As at 150 keV would not exceed 75 nm of penetration (Figure 7b). However, these calculations do not account for the porosity of the VN film. TEM also showed no significant change in the VN film microstructure post-irradiation. From cyclic voltammetry characterization, it was found that unirradiated VN films had the highest capacitance at a scan rate of 2 mV/s, and all samples had quasi-rectangular cyclic voltammograms, characteristic of capacitor behavior. Additionally, the capacitance at 2 mV/s of irradiated samples seemed to decrease with increasing ion irradiation energy. However, the unirradiated VN film seemed to experience more significant capacity fade at higher scan rates compared to the irradiated films (Figure 7c). At a scan rate of 100 mV/s, the CV scan of the unirradiated sample has a shape that indicates resistive behavior, while the irradiated samples maintain quasi-rectangular shapes. The irradiated samples seem to fall into two groups in terms of their capacitive behavior. At 20 and 50 keV the irradiated samples had similar capacitance and EIS curves; the capacitance decreased for the samples irradiated at 100 and 150 keV, though these two samples also had self-similar capacitance values and EIS curves. This seemed to indicate that there may be a threshold energy for improvements in pseudocapacitive behavior at higher scan rates.
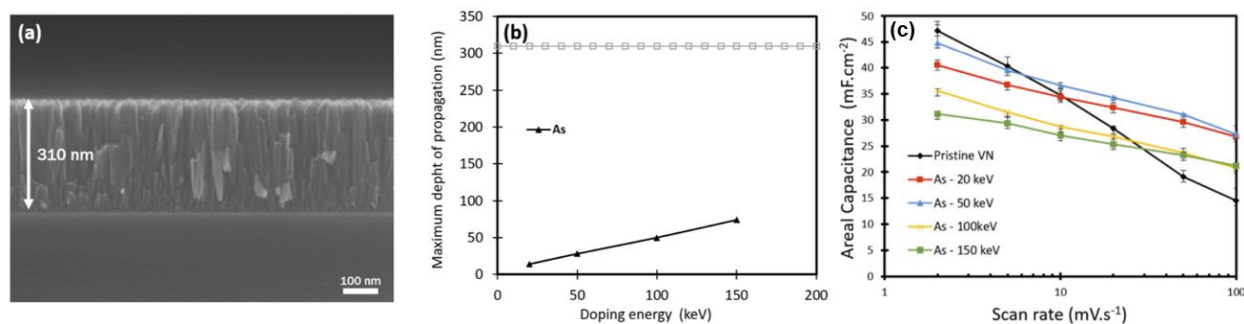
Figure 7. *(a) TEM cross-section of as-prepared of VN films; (b) simulated implantation depth of As ions in VN film as a function of implantation energy, with VN film surface at 0 nm and the horizontal line at 310 nm representing the interface between the Si substrate and the VN film; (c) areal capacitance as a function of scan rate (mV/s) from CV measurements at varying As ion energies. Reproduced from Ref. (62) with permission from Elsevier, copyright 2015.*

The effects of proton irradiation on MnO_2 nanosheets and their electrochemical performance as supercapacitor materials were studied by Lee and coworkers(63). The δ-MnO_2 polymorph was chosen for irradiation due to the inherent 2D layered structures that make it a more feasible material for insertion/extraction sites for electrolytic proton or cationic species. A pellet of δ-MnO_2 was irradiated

with 5.2, 7.8 and 9.8 MeV protons at a current of 200 nA to fluences of 1 x 10^{12}, 1 x 10^{14}, and 1 x 10^{16} protons/cm^2, respectively. XRD and TEM characterization demonstrated that the irradiated δ-MnO$_2$ nanosheets at 7.8 MeV (fluence 1 x 10^{14} protons/cm^2) were exfoliated into a few MnO$_2$ layers that rolled into nanotubes of α-MnO$_2$. At the higher energy and fluence of 9.8 MeV and 1 x 10^{16} protons/cm^2, the irradiated δ-MnO$_2$ nanosheets became completely distorted with both tiny nanosheets and shortened nanorods of α-MnO$_2$. XPS results demonstrated that the O1s peak decreased with respect to proton beam irradiation. The authors determined this was due to O defects in the crystal lattice resulting from irradiation, with the maximum concentration of O defects induced by the highest proton fluence. Raman spectra showed additional peaks at 184 and 573 cm^{-1} that formed when irradiated at 9.8 MeV to a fluence of 1 x 10^{16} protons/cm^2. These peaks are indicative of the external vibration that occurs from the translational motion of MnO$_6$ and the displacement of O atoms relative to the Mn atoms along the octahedral chains. The electrochemical performance was evaluated among the low energy low fluence (7.8 MeV at 1 x 10^{14} protons/cm^2), high energy high fluence (9.8 MeV at 1 x 10^{16} protons/cm^2), and control samples. Rate and cycle performance were both evaluated showing that the low energy, low fluence sample had the best rate performance. The cycle performance of the low fluence, low energy sample matched that of the control. For all the electrochemical studies the high energy, high fluence sample showed the worst performance.

Polymer electrodes, specifically polypyrrole films doped with LiClO$_4$, were irradiated with 160 MeV Ni^{2+} to fluences of 5 x 10^{10}, 5 x 10^{11}, and 3 x 10^{12} ions/cm^2, for an all-polymer redox supercapacitor by Hussain et al(64,65). The authors utilized UV/vis to infer conductivity as a function of fluence as they claimed the intensity of absorption is directly proportional to the quantity of carrier present in the polymer. As the fluence increased the intensity of the peaks at 320 and 440 nm representing the $\pi - \pi^*$ transition of the heteroaromatic pyrrole ring and the polaron absorption peak of pyrrole, both increased indicating that the carrier concentrations increased with irradiation dose. XRD demonstrated that with higher fluences the crystallinity of the polymer films increased. Measurements of conductivity showed an increase with irradiation that the authors claimed stemmed from bond breaking during cross-linking and chain scission, when there were many free electrons. Additionally, irradiation-induced defect sites contributed to the higher conductivity. The supercapacitors were constructed in a symmetrical cell with polymer films on both sides of the cell. Following 10,000 cycles, the sample irradiated to a fluence of 5 $\times 10^{11}$ ions/cm^2 maintained the best capacitance followed by the other irradiated samples. Though initially the unirradiated sample demonstrated the highest capacitance, the capacitance dropped below that of the irradiated samples after ~1500 cycles.

3.2. Interface Engineering

The electrode/electrolyte interface is critical to EES performance. During LIB cycling, the repeated Li$^+$ insertion/extraction can lead to internal stress buildup in the electrodes, which can eventually lead to fractures and crack propagation(66). Three major fracture types can occur: fracture of the active material layer, interfacial delamination, and fracture of metallic foils such as Li or Na metal. Loss of capacity due to electronically disconnected regions, increased impedance of electronic and ionic transport, and intergranular fracture leading to poor ionic and electronic contact between particles are some of the consequences of cracking and fracture (67). Ion irradiation may mitigate these undesirable effects. In some cases, the fracture propensity of electrode materials may be improved by creating a sintered region at the interface. Though cracks may continue to form, the irradiation-enhanced adhesion between the electrode and current collector can improve their electrochemical performance.(23–25)

Of the energy materials known to form cracks or fractures Ge and Si in particular, are of interest. Ge and Si based electrodes promise high theoretical capacity, but their biggest limitation is due to the large volume change that causes significant stress in the electrode, which eventually leads to fragmentation and pulverization of electrode particles upon cycling. The following works have investigated usage of

irradiation to maintain electrical conductivity of the anode materials to demonstrate improved electrochemical performance. Nanostructured Ge films were created by irradiating amorphous Ge films with self-ions at room temperature for use as an anode in LIBs by Rudawski and coworkers.(23) The amorphous Ge films were grown on Ni foil substrates that served as current collectors at a rate of 0.5 nm/s. Subsequently, the films were irradiated with 260 keV Ge$^+$ to a fluence of 1 x 10^{16} ions/cm^2 creating a porous nanoscale interdigitated network of strands that remained amorphous following irradiation. The irradiated samples initially showed a specific discharge capacity of 1259 mAh/g, with no capacity fade after 25 cycles at a rate of C/7.2 (Figure 8a). By comparison, the non-irradiated sample experienced a ~200 mAh/g capacity drop from similar initial capacity following 25 cycles. Additionally, during a rate study when cycling at a rate of ~1.1C, the capacity of the irradiated sample remained greater than 1000 mAh/g (Figure 8b). The authors suggest the difference in performance may be due to all the mass of the electrode remaining in excellent electrical contact with the current collector. This implies that loss of electrical contact due to fracturing or delaminating at the electrode/current collector interface was avoided. These fractures and cracks are known to create electrically non-conductive regions owing to loss of capacity and performance. Consequently, SEM confirmed that the irradiation-induced nanostructuring disappeared during cycling, and cracking occurred after 8 cycles, with the degree of cracking increasing through 16 cycles. Cross-sectional SEM similarly showed increased roughness of the electrode near crack edges appearing at 8 cycles, which increased up through 16 cycles. HR-TEM showed that the nanostructured network no longer existed following 25 cycles (Figure 8c-d). Though cracking occurred in the electrode during cycling, the authors attributed the improved electrochemical performance to a sustained electrical connection of the electrode with the current collector. They suggest this to be due to electrochemical sintering as well as improved adhesion of the electrode to the current collect. The authors compared these results to those of the non-irradiated samples, showing that the entire Ge film delaminated from the Ni foil substrate, whereas no delamination was observed for the irradiated Ge film.
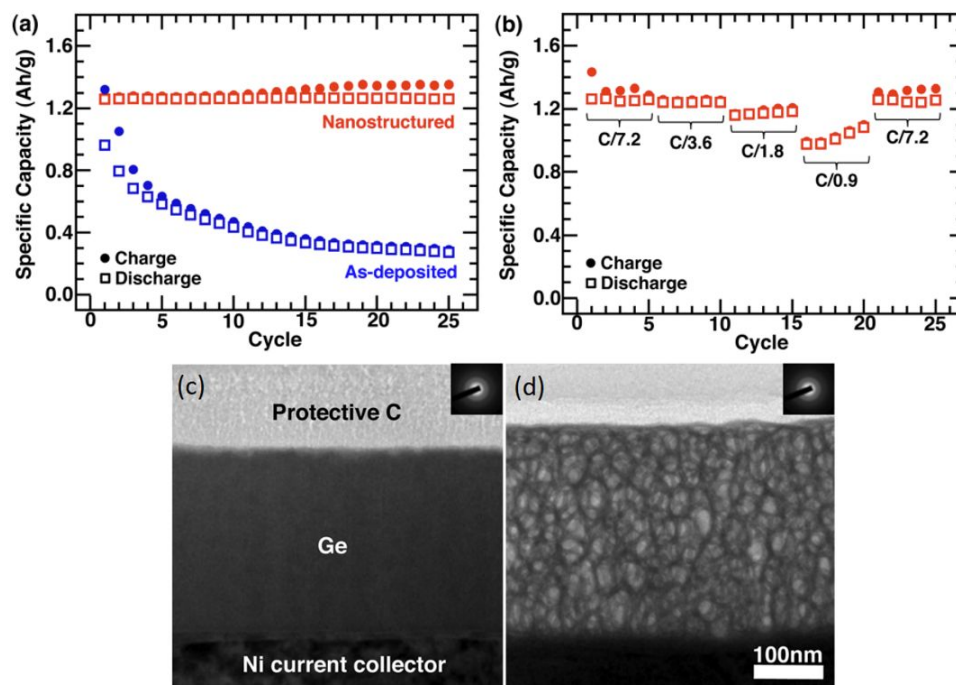

Figure 8. *(a) Specific capacity for the as-deposited and irradiated/nanostructured Ge electrode cycled at a C/7.2 rate through 25 cycles; (b) specific capacity for the irradiated/nanostructured Ge electrode at varied rates; corresponding HR-TEM images with inset SAED pattern of (c) as deposited and (d)*

irradiated/nanostructured Ge film. Reproduced from ref. (23) *with permission from American Institute of Physics, copyright 2012.*

In a study of Si thin-film negative electrodes for LIBs, Deng et al. hypothesized that La ion irradiation via plasma immersion ion implantation could improve cycling performance by increasing adhesion between the Si film and the underlying Cu substrate.(24) SEM analysis of unirradiated and irradiated Si films showed that the lithiated unirradiated film exhibited significant cracking due to internal stresses caused by volume expansion, while the La irradiated lithiated sample exhibited no sign of fracture. Analysis of the electrochemical cycling performance also indicated improvements in cycling stability after 15 cycles. The authors of this study proposed that film adhesion may have been improved via two possible mechanisms: (1) La implantation led to the formation of strong Si-La-Cu bonds at the Si/Cu interface and/or O-La-O bonds that increased the interfacial adhesion between the Si film and the Cu substrate; or (2) ion implantation led to an increase in defect concentration at the Cu foil interface that facilitated diffusion and bonding of Si and Cu atoms, and a subsequent relaxation of mechanical stresses caused by reactions between Li and Si.

Lee and coworkers utilized electron irradiation to cross-link hydride-terminated Si nanocrystals and polyvinylidene fluoride (PVDF), enhancing battery performance.(25) Si-based electrodes promise high theoretical capacity, but are limited by the large volume change that introduces significant stress in the electrode and eventually leads to fragmentation and pulverization during cycling. Lee et al. proposed that electron irradiation would create a crosslinked structure between the Si nanoparticles and the PVDF to limit cracking. Three materials were synthesized: silica nanoparticles (SiO_2 NPs), oxide-coated Si nanoparticles (Si NCs@SiO_x), and hydride terminated Si nanocrystals (H-Si NCs). These synthesized nanomaterials were mixed in slurry with PVDF, super P with N-Methyl-2-pyrrolidone (NMP), and screen printed on a Cu substrate. Samples were irradiated with 1 MeV electrons at a current of 1.2 mA over 90 sec to a dose of 200 kGy. Characterization was completed through SEM, XRD, Fourier-transform infrared spectroscopy (FT-IR), Raman spectroscopy, and thermogravimetric analysis (TGA). Following electron irradiation, PVDF and the H-Si NCs exhibited increased cross-linking. The other two nanomaterials showed no evidence of increased cross-linking following irradiation, and in fact, some existing cross-links between the PVDF-binder system were broken by electron irradiation (Figure 9a-f).
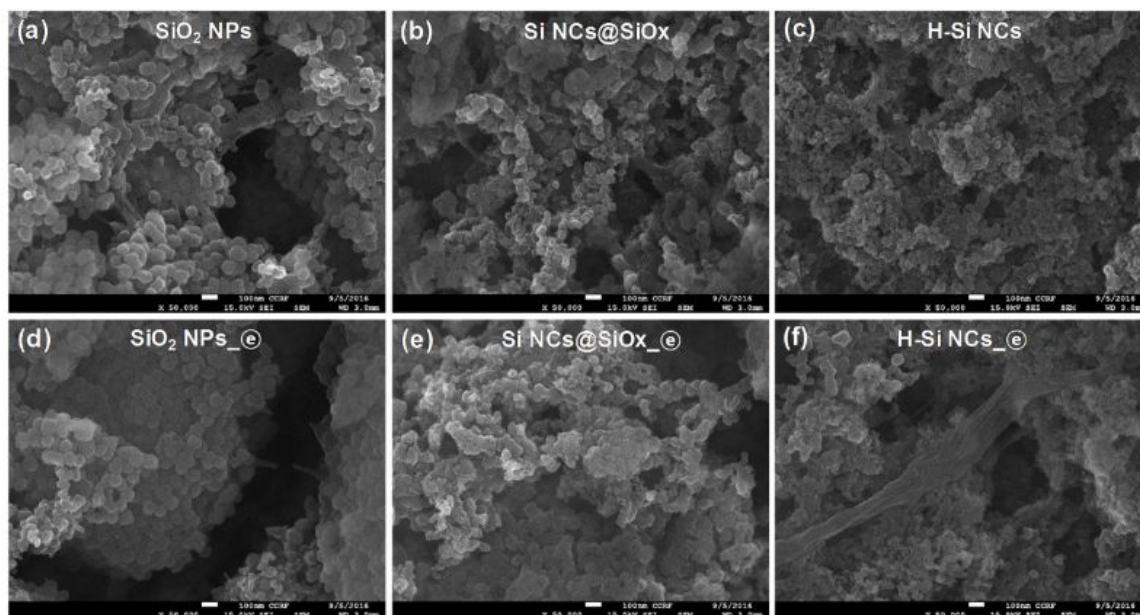
Figure 9. *SEM images of (a-c) unirradiated SiO₂ NPs, Si NCs@SiOx, and H-Si NCs, and (d-f) electron irradiated SiO₂ NPs, Si NCs@SiOx, and H-Si NCs, respectively. Reproduced from Ref. (25) with permission from Elsevier, copyright 2017.*

Lee and coworkers' electron irradiated nanostructured Si-PVDF materials were also evaluated for their electrochemical performance (25). Minor irradiation-induced improvements in electrochemical performance were found in the Si NCs@SiO$_x$ and SiO$_2$ NPs samples, but dramatic improvement in performance was seen for H-Si NCs (Figure 10). For H-Si NCs, the first cycle discharge specific capacity was ~2000 mAh/g and ~600 mAh/g for the irradiated and non-irradiated specimens, respectively. After 100 cycles the irradiated sample demonstrated significant capacity retention (~450 mAh/g) as compared to the non-irradiated sample (<100 mAh/g). Similarly, the rate performance was also greater for the irradiated sample than for the non-irradiated sample. This performance improvement is credited to the cross-linked system that formed in the H-Si NCs sample with PVDF, which induced the formation of a network structure. The authors suggested that improved binding among the Si-Si, Si-binder, or Si-current collector might facilitate better electron/ion transport. EIS was also conducted; the fitted results of the H-Si NCs showed that the R$_{sei}$ value decreased from 447.1 to 204.9 Ω after electron irradiation. The authors explained that this change represents the stabilization of the SEI layers and the less-hindered Li-ion conduction induced by the cross-linked PVDF and H-SI NCs anode. The chemical bond between the Si and C in the PVDF and H-Si NCs minimizes the separation of binder from the active material during cycling, leading to better control over the decomposition of the electrolyte. Post-cycling SEM analysis of the H-Si NCs samples showed evidence of cracks forming in the non-irradiated samples, whereas the irradiated samples showed a smooth surface with uniform distribution of the Si active materials. The authors assert that this further provides evidence that the formation of the chemical bonds between the H-Si NCs and PVDF binders allow for better
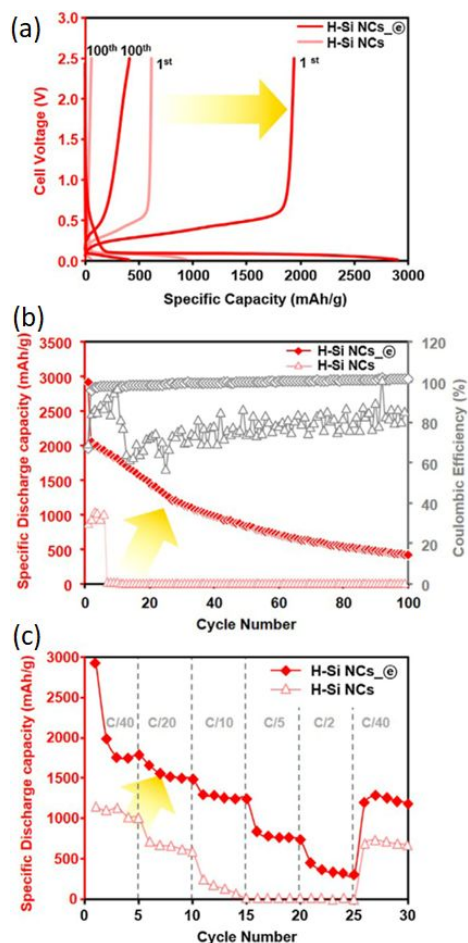
Figure 10. *(a) The first and 100th cycle voltage profiles of H-Si; (b) cycling performance and Coulombic efficiency of H-Si; and (c) rate performance of H-Si NCs based half-cells, where 1C = 4.2 A/g Si. Reproduced from Ref.* (25) *with permission from Elsevier, copyright 2015.*

3.3. Irradiation-Induced Degradation

While the previous sections have focused on irradiation-enhanced or irradiation-tailored battery performance using charged particles (e.g., protons, ions, electrons), studies exploring the effects of uncharged particles (e.g., gamma or neutron irradiation) materials have generally shown that irradiation results in undesirable effects such as capacity loss, reduction in cycle life, and reduced rate capability.(26–31) Such irradiation-induced degradation of batteries and capacitors is especially relevant to applications in high-dose irradiation environments such as unmanned probes vehicles used for space exploration or devices used inside or in proximity of nuclear reactors, and will be the focus of this section.

The effects of gamma irradiation on the electrochemical performance of commercially available LIBs has been reported on by Qiu et al.(29) . Gamma irradiation of the LIB full cells utilizing $LiCoO_2$ as the cathode and graphite as the anode was performed at doses of 0.098, 0.706 and 2.744 Mrad. Analysis from atomic force microscopy (AFM) found that $LiCoO_2$ particle grain size and surface roughness increased with increasing gamma dose (Figure 11a), while electrochemical performance degraded (Figure 11b). The gamma-induced capacity decrease was primarily attributed to the observed grain coarsening. In another study, gamma irradiation was used by Ding et al(68) to irradiate $LiCoO_2$ cathodes, and caused a loss in discharge capacity. The samples were irradiated with γ-rays in air and in Ar to evaluate the role of

oxidation states. Raman spectroscopy showed a peak shift to higher wave numbers for specimens irradiated in air suggesting greater crystallinity, whereas with the specimens irradiated in Ar were shifted in the opposite direction. Analysis of XRD peak ratios elucidated cation disordering in irradiated samples by considering the relative intensities of (003) and (104) peaks. The greater the I_{003}/I_{104} ratio, the more ordered occupation the cations (Li^+ and Co^{3+}) have in the lattice and the lower degree of cation mixing. The sample irradiated in air had a higher I_{003}/I_{104} ratio than the pristine sample (1.95 versus 1.90), indicating more ordered cation occupancy, which was attributed to the conversion of some of the Co^{3+} to Co^{2+} when irradiated. The sample irradiated in Ar showed a lower I_{003}/I_{104} ratio of 1.76, with more cation mixing. The charge-discharge curves showed that the air irradiated and pristine sample had similar capacities of ~133 mAh/g, while the sample irradiated in Ar had a lower capacity of 113 mAh/g. Impedance studies revealed the poorest impedance for the sample irradiated in Ar, followed by the sample irradiated in air. Therefore, gamma irradiation under either ambient atmosphere or inert Ar atmosphere seemed to decrease electrochemical performance by increasing impedance of the $LiCoO_2$ cathode. The cathode irradiated under Ar exhibited higher cation disordering than the sample irradiated under air. The authors suggest that this is due to greater concentrations of oxygen vacancies, and more occupancy exchange of Li and Co cations when the $LiCoO_2$ cathode is irradiated under inert Ar atmosphere.
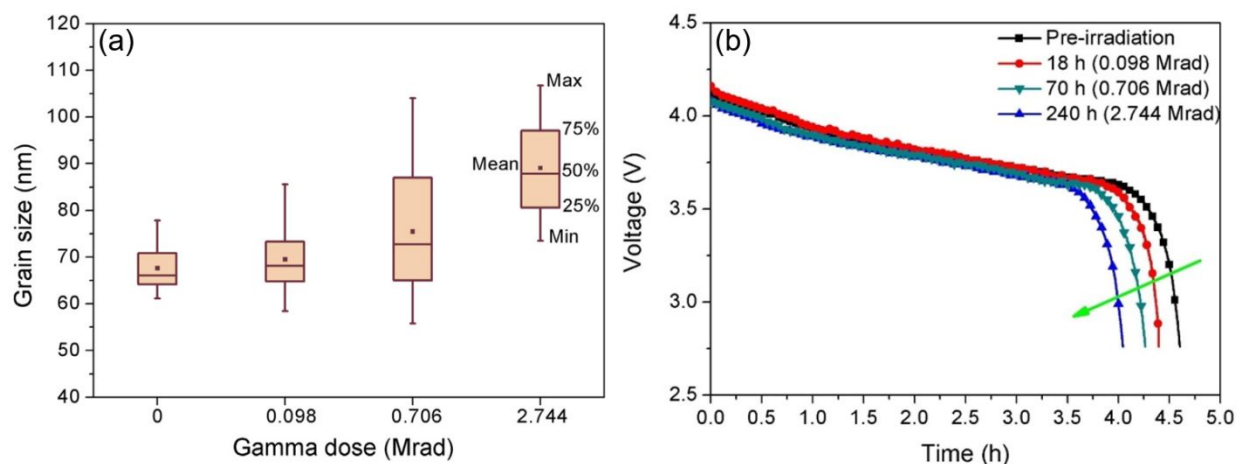
Figure 11. *(a) Grain size measurements of $LiCoO_2$ particles as a function of gamma irradiation dose, with (b) discharge profiles comparing performance of commercial LIBs at various gamma doses. Reproduced from ref. (29) with permission from Elsevier, copyright 2015.*

In a similar study, Tan and coworkers reported on the degradation effects of gamma irradiation on LIBs and separately evaluated the effects of irradiation on the electrolyte and solid cathode materials.(30) LIBs were constructed using an Li-metal anode and a $LiFePO_4$ cathode with 1.0 M $LiPF_6$ in 1:1 ethylene carbonate (EC):dimethyl carbonate (DMC) solution. Cathodes were irradiated to 0.8, 4.1, and 9.8 Mrad, while the liquid electrolyte was irradiated to 0.8, 1.6, and 5.7 Mrad. Discharge curves of coin cells using irradiated electrolyte and pristine cathodes showed decreasing capacity with increasing gamma dose. Discharge curves for batteries constructed using irradiated cathodes also showed decreasing capacity with increasing dose, but the capacity decrease was more pronounced. Additionally, cells made using either irradiated electrolyte or irradiated cathodes had higher failure rates (43-71%) than unirradiated control group cells (~14%). Both gamma irradiated Li-metal batteries, and batteries made with exhibited greater resistance than pristine batteries. The authors attributed the observed decrease in battery performance and increased resistance primarily to irradiation damage of the electrode materials, and chemical reactions in the electrolyte such as polymerization, hydrofluoric acid formation, and bond breakdown of DC/EMC.

The same group also investigated irradiated commercial batteries containing an $LiMnO_2$ cathode and Li-metal anode and in-house constructed cells containing a $LiFePO_4$ cathode and Li-metal anode.[28] These batteries were exposed to either a thermal neutron flux ranging from 9.5 x 10^4 to 7.6 x 10^6 n/cm²s or concurrently with gamma rays and thermal neutrons at doses ranging from 0.027 to 2.133 Rad/h. While undergoing irradiation, the DC battery current was measured; a Cd sheet was inserted to filter thermal neutrons so that the effect of gamma rays and neutrons on current could be separately evaluated. The current increased by ~40 pA at a gamma dose of 2.133 Rad/h, with diminishing increases at lower doses. Thermal neutrons (~0.025 eV) reduced current by ~5 pA at a concurrent fluence of 7.6 x 10^6 n/cm², so gammas had a relatively higher influence on the change in current than did neutrons. The mechanism proposed for the observed current change was that gamma irradiation tends to strip Li of electrons, creating additional Li^+ ions, while neutron collisions consume Li^+ ions via neutron capture events and thus have a negative effect on current. The authors also investigated the effects of neutron and gamma irradiation on commercially available LIBs.[29] Irradiation with both fast (~1 MeV or higher) plus thermal neutrons, or with thermal neutrons alone, caused $LiCoO_2$ particles to increase in size. Particle size and surface roughness also increased with increasing neutron fluence. While the effects on battery performance of neutron irradiation went unexamined in this study, corresponding decreases in capacity were observed alongside similar increases in particle size under gamma irradiation.

Finally, Li et al. investigated the effects of neutron irradiation on the electrochemical performance of Sn negative electrodes fabricated via electrodeposition on Cu.[31] Irradiation was carried out to neutron fluences of 1 x 10^{11}, 1 x 10^{12}, 1 x 10^{13}, and 1 x 10^{14} n/cm². Neutron energy ranged from thermal to fast. XRD analysis showed no significant changes in phase composition, but a shift in d-spacing was observed at a fluence of 1 x 10^{14} n/cm², which could indicate lattice distortion in the crystal structure of the Sn electrodes. SEM showed no significant morphological changes to the electrode surface at a fluences between 1 x 10^{11} - 1 x 10^{13} n/cm², but at 1 x 10^{14} n/cm² voids caused by vacancy clusters and Sn grain growth were apparent. Rate capability measurements showed that capacity of the Sn electrode was degraded by neutron irradiation, with the capacity fade being most pronounced at 1 x 10^{14} n/cm². Rate capability studies also showed worse rate capability and specific capacity as fluence increased, with the 1 x 10^{14} n/cm² irradiated sample being the most degraded. The authors concluded that neutron irradiation degraded electrochemical performance of Sn negative electrodes due to the evolution of vacancies and dislocations and a corresponding increase in grain size and roughness.

3.4. Irradiation-Assisted Synthesis

In some reported work, researchers also utilized irradiation as a means to synthesize novel materials for use in EESs. Effects such as bond breaking, cross-linking, electron excitation, and localized heating may all be accomplished via irradiation techniques to obtain desirable interactions within materials. In particular, during ion irradiation, ions lose their kinetic energy through nuclear and electronic stopping in the target material, which can produce bond breaking and defects that may be utilized for material synthesis. Other methods of irradiation such as electron, microwave, and plasma-jet irradiation do not cause bond breaking, but can instead transfer energy to the target *via* localized heating or electronic excitation which can promote interactions or bonding with other atoms within range.

Saikia and Kumar et al. investigated the ionic conductivity of poly(vinylidenefluoride-co-hexafluoropropylene)-based (PVDF-HFP) gel polymer electrolytes irradiated with 70 MeV C ions at fluences between 5 x 10^9 to 1 x 10^{12} ions/cm².[69] Ionic conductivity increased as a function of ion fluence through 1 x 10^{11} ions/cm², but decreased below the conductivity of the unirradiated control sample at higher fluences. The authors hypothesized that at lower fluences, bond breaking and scission of polymer chains was favored, which led to higher porosity, and therefore higher ionic conductivity due to better incorporation of the liquid electrolyte. Meanwhile, fluences higher than 1 x 10^{11} ions/cm² provided the necessary activation energy for crosslinking and recrystallization of the polymer electrolyte, and

correspondingly decreased ionic conductivity. This explanation was supported by XRD and FTIR results showing evidence of bond breaking and decreased crystallinity at a fluence of 5×10^9 ions/cm^2, with evidence of crosslinking and increased crystallinity at a fluence of 1×10^{12} ions/cm^2.

The effect of N ion implantation on the ionic conductivity of solid lithium phosphorus oxynitride (LiPON) electrolyte film was investigated by Kim et al(70). The 100 keV N ions were implanted at fluences of 2.06×10^{16}, 3.09×10^{16}, and 4.12×10^{16} ions/cm^2 for N at% loadings of 1, 1.5, and 2%, respectively. Although the authors sought to determine whether non-equilibrium N implantation would enhance N crosslinking – and therefore increase ionic conductivity – results were rather inconclusive. EIS measurements indicated that ionic conductivity of LiPON was not significantly changed after N irradiation, and there was no obvious trend between increasing N fluence and ionic conductivity.

Electron irradiation at 2 MeV to 380 kGy was used to synthesize TiO_2 nanoparticle distributions that exhibited enhanced performance.(71) The electron irradiation resulted in nanoparticles with a narrower size distribution (~100-200 nm) compared to the control (~100-500 nm), and greatly repressed agglomeration (Figure 12a-b). The irradiation-induced decrease in size distribution and agglomeration was likely caused by energy from the electron beam overcoming the weak van der Waals forces that lead to the formation of agglomerations during hydrolysis. Additionally, electrons may have eliminated hydroxyl radicals and therefore suppressed agglomeration of nanoparticles. From analyses of voltage profiles, the irradiated TiO_2 nanoparticles had similar first discharge capacity as the unirradiated samples (198.36 mAh/g and 197.67 mAh/g, respectively). However, the irradiated nanoparticles had enhanced charge capacity and better rate capability (Figure 12c), owing to their smaller particle size and narrower particle size distribution which decreased the diffusion length for Li ions. Additionally, the more homogeneous arrangement of TiO_2 active materials improved electrical contact through the electrode.
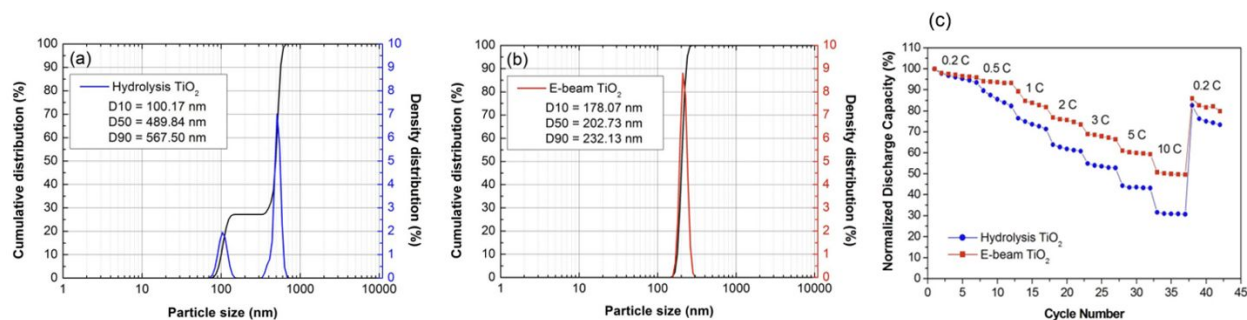

Figure 12. *Particle size distributions of TiO_2 nanoparticles synthesized by (a) hydrolysis and with (b) electron beam irradiation; (c) comparative rate study of hydrolysis and electron irradiation synthesized TiO_2 nanoparticles. Reproduced from ref.* (71) *with permission from The Korean Electrochemical Society, copyright 2015.*

Gamma irradiation has been used to synthesize Fe_3O_4/reduced graphene oxide nanocomposites in LIBs by Liang et al(72). Graphene oxide (GO) was initially synthesized from natural graphite flakes by a modified Hummers method(73). Subsequently, the GO was prepared as an aqueous suspension with $FeCl_3 \cdot 6H_2O$, then exposed to gamma irradiation in a ^{60}Co source at a dose rate of 170 Gy/min. Cells of Fe_3O_4 and the nanocomposites were cycled within a voltage range of 0.01-3.0 V. Nanocomposites were labeled as Fe_3O_4/gGO-1, Fe_3O_4/gGO-2, Fe_3O_4/gGO-3, and Fe_3O_4/gGO-4 depending on the nominal amount of GO they contained. Electrochemical characterization was completed on bare Fe_3O_4 and the nanocomposites to compare their performance following synthesis with gamma irradiation. Fe_3O_4 performed poorest when cycled at current densities of 50 mA/g and 500 mA/g. All other composites synthesized with gamma irradiation demonstrated improved performance. Fe_3O_4/gGO-2 demonstrated the longest sustained specific capacity of all the nanocomposite cells. The authors explain the initial loss of capacity of the nanocomposites due to rGO having less theoretical capacity, as well as forming SEI causing irreversible

capacity loss that stabilizes the cells. At low current densities, Fe_3O_4/gGO-3 and Fe_3O_4/gGO-4 performed poorly due to the formation of a thicker SEI demonstrating lower capacities and capacity fade. At higher current densities, neither Fe_3O_4/gGO-3 nor Fe_3O_4/gGO-4 had enough time to participate in side reactions and thus their capacities were higher with less capacity fade.

Another example of gamma irradiation synthesis to enhance electrochemical performance was conducted by Degheidy et al. on MnO_2 functionalized carbon nanotube PVDF/Ag composites.[74] Gamma irradiation was performed on Ag^+ containing PVDF binder solution to a dose of either 50 or 70 kGy at a dose rate of 1.2 kGy/h in order to form PVDF binder containing Ag-PVDF nanoparticles. The modified binder was then used to prepare laminated electrodes containing the MnO_2 functionalized carbon nanotube active material. The purpose behind modifying the binder in this way was to increase the electrical conductivity of the final electrode material and improve its capacitance. The starting morphology of the battery materials in Figure 13a-h. In Figure 13g-h, the lighter colored particles are Ag nanoparticles distributed in the electrode matrix. The incorporation of the gamma irradiated binder significantly improved the specific capacitance of the material at both low and high CV scan rates when compared to electrodes made using unmodified PVDF, Figure 13i. The Ag-PVDF irradiated at 50 kGy had the highest capacity at all scan rates, while the 70 kGy sample had the second highest capacity; this was attributed to an increase in surface area and active sites for faradaic reactions due to incorporation of the Ag-PVDF nanoparticles.
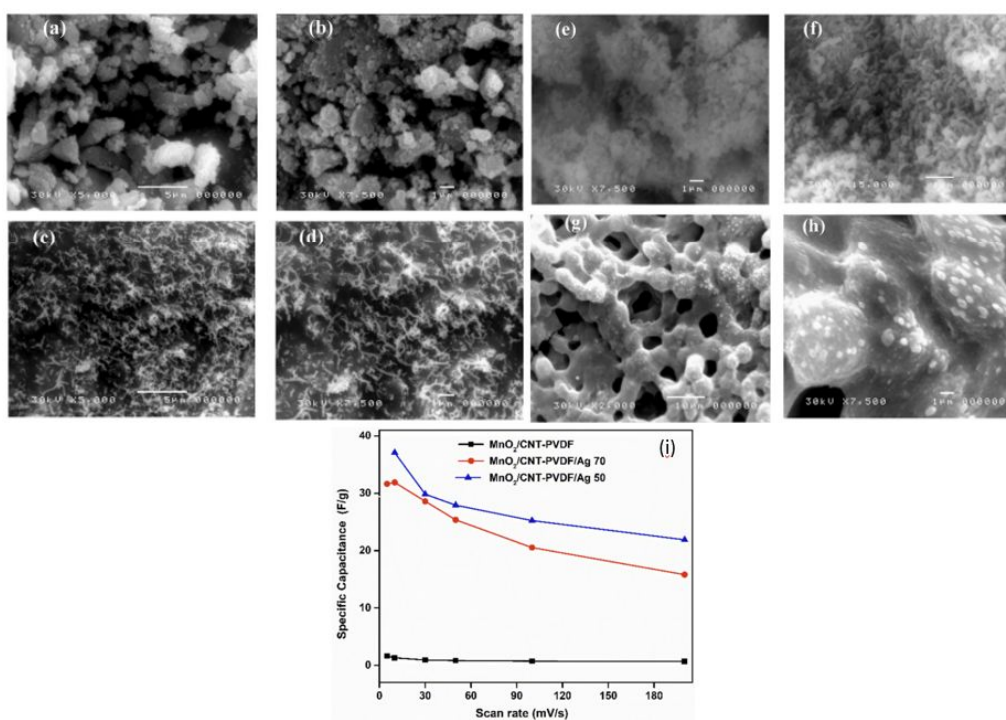
Figure 13. *SEM images of gamma irradiation synthesized composites at higher and lower magnifications: (a-b) MnO_2 active material, (c-d) functionalized CNTs, (e-f) MnO_2/CNT nanocomposite, (g-h) final electrode with Ag-PVDF binder; (i) specific capacitance of composites at various CV scan rates, where "Ag 50" and "Ag 70" refer to PVDF binder irradiated with gamma rays at 50 and 70 kGy, respectively. Reproduced from ref.* (74) *with permission from the Elsevier, copyright 2022.*

Separators were modified by Ma et al. with gamma irradiation to make functionalized polyethylene (PE) by creating active sites on the polymer chain to promote grafting polymerization with 4,4,5,5-tetramethyl-

2-vinyl-1,3,2-dioxaborolane as the monomer(75). PE samples were prepared at 5, 15, and 30 wt% of 4,4,5,5-tetramethyl-2-vinyl-1,3,2-dioxaborolane, referred to as PE-g-B-5, PE-g-B-15, and PE-g-B-30, respectively. Samples were then exposed to gamma irradiation in a ^{60}Co source to a dose of 10 kGy. FT-IR and TG curves were utilized to ensure that the PE became functionalized during irradiation. SEM imaging showed that the separators maintained their porosity throughout irradiation (Figure 14a-d), while EDS data confirmed that the functionalized regions were evenly spread among the PE separator even amongst single strands (Figure 14e-l). EIS was conducted on stainless steel/separator/stainless steel cells and revealed that the ionic conductivity decreased with increasing percentages of functionalized PE. The authors also constructed Li/separator/Li cells to assess Li-ion conductivity, since Li$^+$ is the only species which can participate in electrochemical reaction in the energy conversion process. The Li$^+$ conductivities and Li transference numbers increased with increasing irradiation dose (i.e., functionalization). This improvement of Li$^+$ conductivity may be beneficial for high rate performance due to improved mass transfer stemming from the B atom in the grafted borane molecule providing an active site for reduced solvation restricting movement of PF$_6^-$ in the electrolyte. Half-cells with LiFePO$_4$ and Li metal were constructed and a rate study showed that at low rates PE and PE-g-B-15 performed the same, though at high rates of 5C and 10C the PE-g-B-15 demonstrated a specific discharge capacity (Figure 14). At 10C, PE-g-B-15 shows a capacity of 100 mAh/g whereas the PE shows a capacity of 80 mAh/g. Impedance studies also demonstrated that PE-g-B-15 had lower resistivity than PE due to the borane molecule in the ion conduction path reducing the interface impedance.
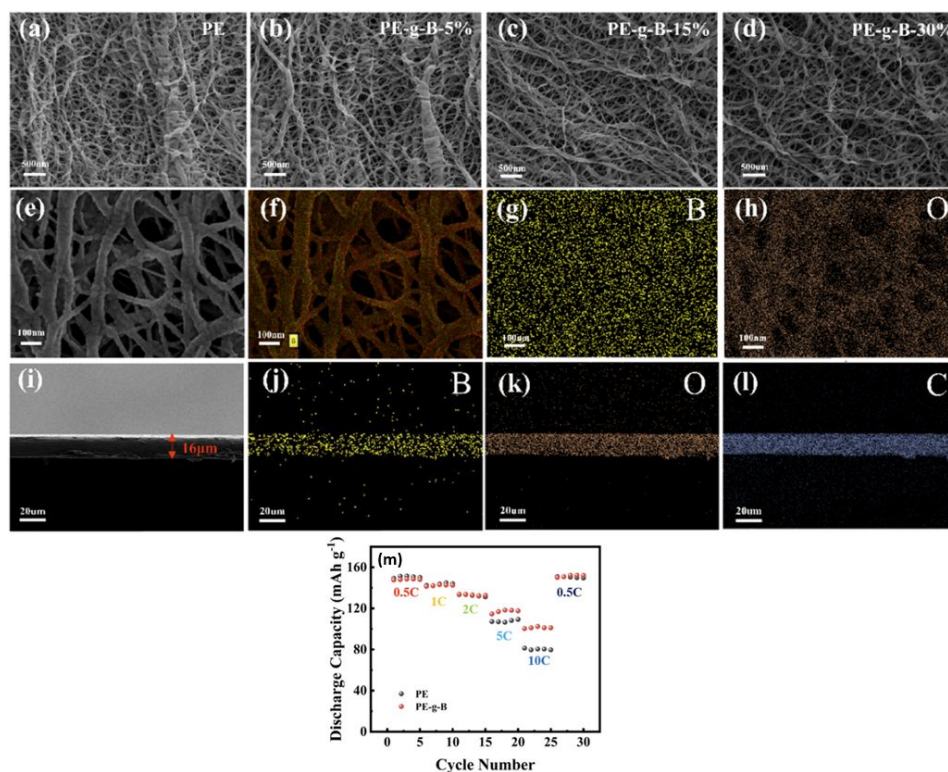
Figure 14. (a-d) *SEM images of the pristine PE separator and gamma irradiated PE separators with various wt% loading of borane; (e-h) EDS elemental mapping of B and O on the surface of the PE-g-B modified separator, and (i-l) of B, O, and C for the cross-section of the PE-g-B modified separator; (m) discharge C-rate capabilities of LiFePO$_4$ half-cells assembled with pristine PE separators and borane-modified PE separators. Reproduced from ref.* (75) *with permission from American Chemical Society, copyright 2021.*

Similar work on separators activated by gamma irradiation for use in LIBs was completed by Sheng et al.(76) The PE separators were irradiated with ^{60}Co gamma rays at doses of 20, 40, 60, 80, and 100 kGy all at a dose rate of 0.57 kGy/h. The irradiation removed H from the surface C chains of the PE by forming radicals and becoming oxidized. FTIR-ATR characterize the functionality developed on the irradiated PE, and showed the formation of new peaks at 1029-1350 cm^{-1} and 1700-1730 cm^{-1} which are associated with C-O and C=O functional groups. TGA showed that the melting points decreased with increasing irradiation dose due to weakened Van der Waals forces associated with the long PE chains breaking. The electrochemical cycling performance of the separators showed that the PE cell began to lose capacity following ~30 cycles much more dramatically than the 20 kGy irradiated PE ("PE-20"). The rate studies used both symmetrical and asymmetrical cycling. The unirradiated control and PE-20 performed similarly during symmetrical cycling, but the PE-20 exhibited improved performance over the unirradiated control during asymmetrical cycling. The authors attributed this increase in battery performance to the gained affinity of the separator to liquid electrolyte. The gamma irradiation treatment increased the polarity of the PE separator, improving the interface compatibility between the Li metal anode and electrolyte.

In-situ bulk synthesis of holey reduced graphene oxide/polystyrene (HRGO/PS) nanocomposites with 0.1%, 1%, and 2% HRGO concentrations via in-situ polymerization was conducted using microwave irradiation by Aldawsari et al(77). A mixture of styrene, HRGO, and benzoyl peroxide was sonicated for 1 hr, maintained at 60ºC for 20 hrs to promote polymerization, sonicated for an additional 1 hr, then reduced by microwave irradiation. Electrical conductivity studies were conducted on neat PS and HRGO/PS, and showed that neat PS was insulative with an electrical conductivity in the range of 10^{-2} - 10^{-7} S/cm. Electrical conductivity increased when HRGO concentration increased from 0.1% to 1%, but then decreased when HRGO concentration increased further to 2%. The authors suggested that this observation may be explained by the uneven dispersion of HRGO throughout the PS matrix. Additionally, Raman spectroscopy of the 1% HRGO/PS showed larger sp^3 domains when compared to 2% HRGO/PS, and XRD also showed a higher degree of crystallinity in 1% HRGO/PS. Electrochemical studies were conducted on the 1% HRGO/PS by cycling pre-lithiated and non pre-lithiated samples at 100 mA/g with specific discharge capacities of 149.97 and 107.85 mAh/g. The authors explained that this capacity increase in the pre-lithiated sample is due to pre-treatment of the electrode allowing for the prevention of Li loss. EIS showed that the diameter of the charge-transfer resistance in the low frequency range of the pre-lithiated 1% HRGO/PS nanocomposite is slightly smaller than in the non pre-lithiated sample. Rate study capabilities were also evaluated at current densities of 200 to 600 mA/g showing that even at high current densities of 500 mA/g the discharge capacity was about ~60 mAh/g. Cycle studies of 1% HRGO/PS at 500 mA/g showed 100% columbic efficiency at a discharge capacity of 92.78 mAh/g following 20 cycles; at 100 mA/g, initial discharge capacity of 176.17 mAh/g dropped to 119.03 mAh/g after 100 cycles.

Huang et al. studied $ZnCo_2O_4$/ZnO nanocrystal/carbon nanotube (ZZCO/CNT) composite anodes synthesized via microwave irradiation and annealing(78). ZZCO/CNT anodes were made by sonicating multi-walled CNTs in ethanol for 1 hr followed by adding cobaltous acetate, zinc acetate, and concentrated ammonia while stirring. The resulting mixture was reacted at 82ºC and 500 W for 10 min in a microwave oven. The Zn-Co precursor was obtained through centrifugation and calcined at 400ºC in air for 3 hrs. Structural and electrochemical comparisons were drawn between pure ZZCO nanoparticles and ZZCO/CNTs. TEM showed that 5 nm sized ZZCO nanoparticles were anchored on the CNTs; TGA determined the CNT mass fraction in the as-prepared composite was 8.2%. From Raman analysis revealed that the intensity ratio of I_D/I_G for the ZZCO/CNT nanocomposite and the stand-alone CNTs were 0.98 and 1.145, respectively, showing that the ZZCO/CNT nanocomposite had a higher degree of crystallinity. The authors suggested that this greater crystallinity will contribute towards the electronic conductivity of the ZZCO/CNT. Results from the rate study showed that both the capacity and rate performance of the ZZCO/CNTs was greatly enhanced compared to ZZCO. While the specific capacity of

ZZCO remained fairly consistent following 150 cycles at ~220 mAh/g, ZZCO/CNT began to show increased capacity with increasing cycles, reaching ~1450 mAh/g by 150 cycles. The authors ascribed this increase to three reasons. First, the reversible electrolyte decomposition at low voltage results in extra Li-ion adsorption/desorption on the reversible SEI film, providing added capacity. Second, the ZZCO nanoparticles have higher electrochemical activity during cycling due to increased Li-ion intercalation sites. Lastly, Co^{2+} oxidizes in the initial cycles to Co^{3+} after being charged due to improved kinetics, which may allow for higher capacity. The surface area of the CNTs allowed for better penetration of electrolyte and restricted the sides of the ZZCO nanoparticles. This combination of effects allowed for ease of Li-ion intercalation and mitigated volume strains while cycling. Rate studies were also conducted showing that the ZZCO/CNTs had vastly improved rate performance over ZZCO nanoparticles at current densities ranging over 100-3200 mA/g.

Table 1. *Summary of literature reporting irradiation effects in energy materials.*

Material(s)	Type of technology	Energy	Fluence/Dose (ions or neutrons/cm^2), or Fluence/Dose Rate	Classification	Application	Ref
TiO_2 nanotubes	Ion Irradiation w/ H^+	195 keV	2.18×10^{17}	Defect engineering	Battery/Neg. Electrode	(19)
TiO_2 nanotubes	Ion Irradiation w/ H^+	200 keV	2.18×10^{17}	Defect engineering	Battery/Neg. Electrode	(20)
TiO_2 single crystal	Ion Irradiation w/ Nb^+	3 MeV	4.03×10^{11}	Defect engineering	Battery/Neg. Electrode	(21)
Graphite	Ion Irradiation w/ N^+ and C^+	50 keV	1×10^{12}	Defect engineering	Battery/Neg. Electrode	(51)
Si	Ion Implantation w/ Cu	95 keV	7.5×10^{16}	Defect engineering	Battery/Neg. Electrode	(52)
Ni nanotubes	Ion Irradiation w/ Ca^{5+}	68 MeV	$1 \times 10^{10} - 1 \times 10^{11}$	Defect engineering	Battery/Neg. Electrode	(53)
MoS_2	Ion Implantation w/ W and Mo	10 keV	Mo: 1×10^{14}, 1×10^{16}, 2×10^{16}; W: 1×10^{14}, 1×10^{16}, 1×10^{16}	Defect engineering	*Capacitor	(54)
$Na_{2/3}Fe_{1/2}Mn_{1/2}O_2$ and $LiNiO_2$	Ion Implantation w/ Kr	1 MeV	6.25×10^{14}	Defect engineering	Battery/Pos. Electrode	(55)
$Li_4Ti_5O_{12}$	Plasma Jet Irradiation w/ Ar/N_2	100 W	-	Defect engineering	Battery/Neg. Electrode	(47)
$Li_{6.4}La_3Zr_{1.4}Ta_{0.6}O_{12}$	Ion Implantation w/ Xe	50, 80, 150, 190 keV	1×10^{12}, 1×10^{13}, 1×10^{14}	Defect engineering	Battery/Electrolyte	(56)
$Li_4Ti_5O_{12}$	Plasma Jet Irradiation w/ Ar/N_2	300 W	-	Defect engineering	Battery/Neg. Electrode	(60)
TiO_2 nanotubes	Ion Irradiation w/ Ag	60 keV	$0.5 \times 10^{17} - 1 \times 10^{18}$	Defect engineering	Capacitor/Neg. Electrode	(61)
VN thin films	Ion Irradiation w/ As	20-150 keV	1×10^{15}	Defect engineering	Pseudocapacitor	(62)

MnO_2 nanosheets	Ion Irradiation w/ H^+	5.2, 7.8, and 9.8 MeV	1×10^{12}, 1×10^{14}, 1×10^{16}	Defect engineering	Supercapacitor	(63)
Polypyrrole films doped with $LiClO_4$	Ion Irradiation w/ Ni^{2+}	160 MeV	5×10^{10}, 5×10^{11}, 3×10^{12}	Defect engineering	Supercapacitor	(64, 65)
Ge films	Ion Irradiation w/ Ge^+	260 keV	1×10^{16}	Interface engineering	Battery/Neg. Electrode	(23)
Si thin films	Plasma Immersion Ion Implantation w/ La	20 kV	-	Interface engineering	Battery/Neg. Electrode	(24)
Hydride-terminated Si nanocrystals and PVDF	Electron Irradiation	1 MeV	200 kGy	Interface engineering	Battery/Neg. Electrode	(25)
Graphite and $LiCoO_2$	Neutron and Gamma Irradiation	-	Neutron: $10^{12} - 10^{15}$ n/cm^2 Gamma: 0.098, 0.706, 2.744 Mrad	Degradation	Battery	(29)
$LiCoO_2$	Gamma Irradiation	-	144 kGy, 100 Gy/min	Degradation	Battery/Pos. Electrode	(68)
$LiFePO_4$ and $LiPF_6$ electrolyte	Gamma Irradiation	-	0.8 – 9.8 Mrad	Degradation	Battery	(30)
$LiMnO_2$, $LiFePO_4$, Li metal	Neutron and Gamma Irradiation	5-400 kW	Neutron: $9.5 \times 10^4 - 7.6 \times 10^6$ $n/cm^2 *s$ Gamma: $0.027 - 2.133$ rad/h	Degradation	Battery	(28)
Sn	Neutron Irradiation	0.025 eV - ~1 MeV	$1 \times 10^{11} - 1 \times 10^{14}$, $n/cm^2 *s$	Degradation	Battery/Neg. Electrode	(31)
PVDF-HFP	Ion Irradiation w/ C	70 MeV	$5 \times 10^9 - 1 \times 10^{12}$, $1 \times 10^9 - 5 \times 10^{12}$	Synthesis	Battery/Electrolyte	(69)
LiPON	Ion Implantation	100 keV	$2.06 \times 10^{16} - 4.12 \times 10^{16}$	Synthesis	Battery/Electrolyte	(70)
TiO_2 nanoparticles	Electron Irradiation	2 MeV	380 kGy	Synthesis	Battery/Neg. Electrode	(71)
Fe_3O_4/reduced graphene oxide nanocomposites	Gamma Irradiation	-	153 kGy, 170 Gy/min	Synthesis	Battery/Neg. Electrode	(72)
MnO_2 functionalized carbon nanotube PVDF/Ag composites	Gamma Irradiation	50, 70 kGy	50 and 70 kGy, 1.2 kGy/h	Synthesis	Battery/Neg. Electrode	(74)

Polyethylene separators	Gamma Irradiation	-	10 kGy	Synthesis	Battery/Separator	(75)
Polyethylene separators	Gamma Irradiation	20, 40, 60, 80, and 100 kGy	20-100 kGy, 0.57 kGy/h	Synthesis	Battery/Separator	(76)
Holey reduced graphene oxide/polystyrene nanocomposites	Microwave Irradiation	900W	20-100 kGy, 0.57 kGy/h	Synthesis	Battery/Neg. Electrode	(77)
$ZnCo_2O_4$/ZnO nanocrystal/carbon nanotube composite	Microwave Irradiation	500 W	-	Synthesis	Battery/Neg. Electrode	(78)

4. SUMMARY AND OUTLOOK

With the increasing demands for energy storage systems across numerous markets including high projected growth sectors such as vehicle electrification, grid-storage, and aerospace, it is imperative to develop high performance EES materials with improved properties, and to ascertain a comprehensive understanding of their degradation mechanisms. Moreover, future planetary exploration missions beyond Mars may experience more hostile (e.g., lower temperature) and extreme radiative environments that necessitate in-depth understanding of radiation-induced degradation in EESs which could contain solids, organic electrolytes, polymeric binder and separator materials, and their interfaces. This review demonstrates the wide range of effects that radiation can have on EES materials – from offering promise as a synthesis technique, to compromising EES performance. The published works utilizing radiation for defect/interface engineering, synthesis, and investigation of radiation-induced degradation in EES materials are summarized in Table 1. These summarized studies have all been conducted on different materials, using different irradiation types and energies, at different temperatures, and their properties and performance have been characterized using different techniques. This lack of systematic data precludes the emergence of clear trends, let alone unifying theories of behavior; this underscores the need for a controlled series of separate effects studies.

Interpreting these varied effects of radiation on EES materials to gain insights into unifying principles requires us to bridge length scales, from sub-atomic/atomic scale inter-particle interactions, through the resultant nano/microscopic structures. At the atomic scale, radiation can introduce point defects (e.g., Frenkel pair defects, antisite defects, lattice disorder/order) by transferring energy from energetic incident particle through electronic or nuclear interactions, leading to displacement and ionization of atoms. These point defects can subsequently develop into extended 2D defects (e.g., grain/phase boundaries). All of these length scales of radiation "defects" in EES materials have been either theorized or proven in the literature to promote electrochemical charge storage because of the corresponding changes to storage sites, electronic structures, and charge carrier concentrations. Radiation can also be utilized to alter the material surfaces and interfacial properties through modulation of surface groups and by ion beam mixing. Several studies have shown that irradiation-induced degradation of battery materials has a correlation with increased particle size and/or increased grain boundary size – indicating that radiation can have a negative impact on effective surface area of the battery electrodes.(29–31) Additionally, radiation is found to assist in the synthesis of nanostructured EES materials exhibiting improved kinetics.

Compared to progress in other areas for EES, exploration of the radiation effects on EES materials is still in its infancy. The archival literature on radiation effects for EES materials remains limited and non-systematic, with sometimes inconsistent or inconclusive results. A thorough understanding of defect formation and evolution mechanisms under various modes of irradiation remains elusive. Further, there is an even more significant knowledge gap on the precise role of these irradiation defects on the electrochemical properties and performance of EES materials. Some understanding has been obtained for polymeric materials, in which ion irradiation can increase electronic conductivity through doping, modify density, chain length, and solubility, and can also lead to bond breaking, cross-linking, and creation of defects. For battery and EC electrodes, the morphology and size of the irradiated materials have been found to be at least somewhat dependent on irradiation species, energy, and fluence, and sometimes dependent on atmosphere (e.g., for oxygen vacancy formation). There remain limited theoretical studies of radiation effects in EES materials, aside from a few works on defect formation and mechanical properties.

The use of radiation to intentionally engineer defects in EES materials is a promising route toward significantly improving their electrochemical properties. However, fully harnessing this potential requires development of state-of-the-art local and global characterization techniques with high temporal and spatial resolution to qualitatively and quantitatively analyze the generated defects and their evolution.

More conclusive understanding is also necessary to unquestionably elucidate the specific roles of electronic and nuclear stopping and how they affect the resulting structure, microstructure, mechanical, and electrochemical properties. Thermo-kinetics of the phase transitions in the irradiated materials need to be clearly discerned. Conditions that resemble a wide range of extreme environments (e.g., high radiative) should be tested systematically and fundamentally to understand the degradation mechanisms. Radiation on EES materials is an emerging field and has many intriguing areas that remain to be understood. Continued efforts in research of synthesis, processing, characterization, and computational studies are of paramount importance for the success of radiation-assisted defect/interface engineering and EES operations under extreme environments(79,80).

ACKNOWLEDGEMENTS

REFERENCES

1. Ziegler MS, Mueller JM, Pereira GD, Song J, Ferrara M, Chiang YM, et al. Storage Requirements and Costs of Shaping Renewable Energy Toward Grid Decarbonization. Joule. 2019 Sep;3(9):2134–53.

2. Breeze P. Power System Energy Storage Technologies. In: Power Generation Technologies [Internet]. Elsevier; 2014 [cited 2022 Dec 14]. p. 195–221. Available from: https://linkinghub.elsevier.com/retrieve/pii/B9780080983301000107

3. Scrosati B, Hassoun J, Sun YK. Lithium-ion batteries. A look into the future. Energy Environ Sci. 2011;4(9):3287.

4. Wu HB, Lou XW (David). Metal-organic frameworks and their derived materials for electrochemical energy storage and conversion: Promises and challenges. Sci Adv. 2017 Dec;3(12):eaap9252.

5. Xu NN, Li GP, Lin QL, Liu H, Bao LM. Effect of Ar ion irradiation on the room temperature ferromagnetism of undoped and Cu-doped rutile TiO_2 single crystals. Chinese Physics B. 2016 Nov;25(11):116103.

6. Pomerantseva E, Bonaccorso F, Feng X, Cui Y, Gogotsi Y. Energy storage: The future enabled by nanomaterials. Science. 2019 Nov 22;366(6468):eaan8285.

7. Global Energy Storage Market to Grow 15-Fold by 2030 [Internet]. BloombergNEF. 2022 [cited 2023 May 11]. Available from: https://about.bnef.com/blog/global-energy-storage-market-to-grow-15-fold-by-2030/

8. Bruce PG, Scrosati B, Tarascon JM. Nanomaterials for Rechargeable Lithium Batteries. Angewandte Chemie International Edition. 2008;47(16):2930–46.

9. Koo B, Xiong H, Slater MD, Prakapenka VB, Balasubramanian M, Podsiadlo P, et al. Hollow Iron Oxide Nanoparticles for Application in Lithium Ion Batteries. Nano Lett. 2012 May 9;12(5):2429–35.

10. Wang G, Yang Y, Han D, Li Y. Oxygen defective metal oxides for energy conversion and storage. Nano Today. 2017 Apr;13:23–39.

11. Savva AI, Smith KA, Lawson M, Croft SR, Weltner AE, Jones CD, et al. Defect generation in TiO2 nanotube anodes via heat treatment in various atmospheres for lithium-ion batteries. Physical Chemistry Chemical Physics. 2018;20(35):22537–46.

12. Hahn BP, Long JW, Rolison DR. Something from Nothing: Enhancing Electrochemical Charge Storage with Cation Vacancies. Acc Chem Res. 2013 May 21;46(5):1181–91.

13. Koketsu T, Ma J, Morgan BJ, Body M, Legein C, Dachraoui W, et al. Reversible magnesium and aluminium ions insertion in cation-deficient anatase TiO2. Nature Mater. 2017 Nov;16(11):1142–8.

14. Li G, Blake GR, Palstra TTM. Vacancies in functional materials for clean energy storage and harvesting: the perfect imperfection. Chem Soc Rev. 2017 Mar 21;46(6):1693–706.

15. Sun D, Xue X, Tang Y, Jing Y, Huang B, Ren Y, et al. High-Rate LiTi2(PO4)3@N–C Composite via Bi-nitrogen Sources Doping. ACS Appl Mater Interfaces. 2015 Dec 30;7(51):28337–45.

16. Swider-Lyons KE, Love CT, Rolison DR. Improved lithium capacity of defective V2O5 materials. Solid State Ionics. 2002 Dec 1;152–153:99–104.

17. Liu S, Yin Y, Ni D, Hui KS, Ma M, Park S, et al. New insight into the effect of fluorine doping and oxygen vacancies on electrochemical performance of Co2MnO4 for flexible quasi-solid-state asymmetric supercapacitors. Energy Storage Materials. 2019 Nov;22:384–96.

18. Kim G, Feng B, Sheu YM, Cho HJ, Ikuhara Y, Ohta H. Coexistence of High Electron Conduction and Low Heat Conduction in Tungsten Oxide Epitaxial Films with 1D Atomic Defect Tunnels. ACS Appl Electron Mater. 2020 Aug 25;2(8):2507–13.

19. Smith KA, Savva AI, Mao KS, Wang Y, Tenne DA, Chen D, et al. Effect of proton irradiation on anatase TiO2 nanotube anodes for lithium-ion batteries. Journal of Materials Science. 2019 Oct 11;54(20):13221–35.

20. Smith KA, Savva AI, Deng C, Wharry JP, Hwang S, Su D, et al. Effects of proton irradiation on structural and electrochemical charge storage properties of TiO2 nanotube electrodes for lithium-ion batteries. Journal of Materials Chemistry A. 2017;5(23):11815–24.

21. Smith KA, Savva AI, Wu Y, Tenne DA, Butt DP, Xiong H, et al. Effects of intermediate energy heavy-ion irradiation on the microstructure of rutile TiO$_2$ single crystal. Journal of the American Ceramic Society. 2018 Sep 17;101(9):4357–66.

22. Wharry JP, Xiong H (Claire), Olsen T, Yang C. Radiation Effects in Battery Materials. In: Encyclopedia of Energy Storage [Internet]. Elsevier; 2022 [cited 2022 Dec 1]. p. 243–55. Available from: https://linkinghub.elsevier.com/retrieve/pii/B9780128197233001098

23. Rudawski NG, Darby BL, Yates BR, Jones KS, Elliman RG, Volinsky AA. Nanostructured ion beam-modified Ge films for high capacity Li ion battery anodes. Appl Phys Lett. 2012 Feb 20;100(8):083111.

24. Deng HX, Chung CY, Xie YT, Chu PK, Wong KW, Zhang Y, et al. Improvement of electrochemical performance of Si thin film anode by rare-earth La PIII technique. Surface and Coatings Technology. 2007 Apr;201(15):6785–8.

25. Lee DS, Choi YH, Jeong HD. Effect of electron beam irradiation on the capacity fading of hydride-terminated silicon nanocrystal based anode materials for lithium ion batteries. Journal of Industrial and Engineering Chemistry. 2017 Sep 25;53:82–92.

26. Ratnakumar BV, Smart MC, Kindler A, Frank H, Ewell R, Surampudi S. Lithium batteries for aerospace applications: 2003 Mars Exploration Rover. Journal of Power Sources. 2003 Jun;119–121:906–10.

27. Tan C, Bashian NH, Hemmelgarn CW, Thio WJ, Lyons DJ, Zheng YF, et al. Ex-situ and in-situ observations of the effects of gamma radiation on lithium ion battery performance. Journal of Power Sources. 2017 Jul;357:19–25.

28. Qiu J, Cao L, Mulligan P, Turkoglu D, Nagpure SC, Canova M, et al. The Potential of Using Li-Ion Batteries for Radiation Detection. IEEE Transactions on Nuclear Science. 2013 Apr;60(2):662–7.

29. Qiu J, He D, Sun M, Li S, Wen C, Hattrick-Simpers J, et al. Effects of neutron and gamma radiation on lithium-ion batteries. Nuclear Instruments and Methods in Physics Research Section B: Beam Interactions with Materials and Atoms. 2015 Feb 15;345:27–32.

30. Tan C, Lyons DJ, Pan K, Leung KY, Chuirazzi WC, Canova M, et al. Radiation effects on the electrode and electrolyte of a lithium-ion battery. Journal of Power Sources. 2016 Jun 30;318:242–50.

31. Li L, Wu H, Ma Z. Neutron radiation on tin anodes of lithium-ion batteries. Radiation Effects and Defects in Solids. 2018 Dec 2;173(11–12):1068–74.

32. Nagatani K, Kiribayashi S, Okada Y, Otake K, Yoshida K, Tadokoro S, et al. Emergency response to the nuclear accident at the Fukushima Daiichi Nuclear Power Plants using mobile rescue robots: Emergency Response to the Fukushima Nuclear Accident using Rescue Robots. J Field Robotics. 2013 Jan;30(1):44–63.

33. Azevedo CRF. A review on neutron-irradiation-induced hardening of metallic components. Engineering Failure Analysis. 2011 Dec 1;18(8):1921–42.

34. Das S. Recent advances in characterising irradiation damage in tungsten for fusion power. SN Appl Sci. 2019 Nov 15;1(12):1614.

35. Was GS. Fundamentals of Radiation Materials Science: Metals and Alloys. Springer Science & Business Media; 2007. 839 p.

36. Weber WJ, Duffy DM, Thomé L, Zhang Y. The role of electronic energy loss in ion beam modification of materials. Current Opinion in Solid State and Materials Science. 2015 Feb 1;19(1):1–11.

37. Koroni C, Olsen T, Wharry JP, Xiong H. Irradiation-Induced Amorphous-to-Crystalline Phase Transformations in Ceramic Materials. Materials. 2022 Jan;15(17):5924.

38. Backman M, Djurabekova F, Pakarinen OH, Nordlund K, Zhang Y, Toulemonde M, et al. Cooperative effect of electronic and nuclear stopping on ion irradiation damage in silica. J Phys D: Appl Phys. 2012 Nov;45(50):505305.

39. Moisy F, Sall M, Grygiel C, Balanzat E, Boisserie M, Lacroix B, et al. Effects of electronic and nuclear stopping power on disorder induced in GaN under swift heavy ion irradiation. Nuclear Instruments and Methods in Physics Research Section B: Beam Interactions with Materials and Atoms. 2016 Aug 15;381:39–44.

40. Zhang Y, Xue H, Zarkadoula E, Sachan R, Ostrouchov C, Liu P, et al. Coupled electronic and atomic effects on defect evolution in silicon carbide under ion irradiation. Current Opinion in Solid State and Materials Science. 2017 Dec 1;21(6):285–98.

41. Sigmund P. Collision theory of displacement damage. IV. Ion range and sputtering. Revue Roumaine De Physique. 1972;17(8):969–1000.

42. Toulemonde M, Dufour C, Paumier E. Transient thermal process after a high-energy heavy-ion irradiation of amorphous metals and semiconductors. Phys Rev B. 1992 Dec 1;46(22):14362–9.

43. Toulemonde M, Dufour Ch, Meftah A, Paumier E. Transient thermal processes in heavy ion irradiation of crystalline inorganic insulators. Nuclear Instruments and Methods in Physics Research Section B: Beam Interactions with Materials and Atoms. 2000 May 2;166–167:903–12.

44. Krasheninnikov AV, Nordlund K. Ion and electron irradiation-induced effects in nanostructured materials. Journal of Applied Physics. 2010 Apr;107(7):071301.

45. Nelson G, Reilly D. Gamma-Ray Interactions with Matter. Passive Nondestructive Analysis of Nuclear Materials, Los Alamos National Laboratory. 1991;27–42.

46. Matsusaka S. Control of particle charge by atmospheric pressure plasma jet (APPJ): A review. Advanced Powder Technology. 2019 Dec 1;30(12):2851–8.

47. Lin HH, Yang H, Wu CY, Hsu SY, Duh JG. Atmospheric Pressure Plasma Jet Irradiation of N Doped Carbon Decorated on Li4Ti5O12 Electrode as a High Rate Anode Material for Lithium Ion Batteries. J Electrochem Soc. 2018 Dec 5;166(3):A5146.

48. Singh V, Kumar P, Sanghi R. Use of microwave irradiation in the grafting modification of the polysaccharides – A review. Progress in Polymer Science. 2012 Feb 1;37(2):340–64.

49. Singal S, Joshi A, Tomar AK, Sahu V, Singh G, Sharma RK. Vacancies and edges: Enhancing supercapacitive performance metrics of electrode materials. Journal of Energy Storage. 2020 Oct;31:101614.

50. Lu W, Yan L, Ye W, Ning J, Zhong Y, Hu Y. Defect engineering of electrode materials towards superior reaction kinetics for high-performance supercapacitors. J Mater Chem A. 2022;10(29):15267–96.

51. Hai Y, Cui W, Lin Y, Han P, Chen H, Zhu Z, et al. Surface modification of graphite by ion implantation for promoting the electrochemical property in Li-ion batteries. Applied Surface Science. 2019 Aug;484:726–31.

52. Hu ZG, Tan ZY, Lin Z, Chen J, Wang BS, Tian LF, et al. Cu ion implantation improves the performance of Si film anode used in lithium ion battery. Nuclear Instruments and Methods in Physics Research Section B: Beam Interactions with Materials and Atoms. 2019 Feb;440:191–6.

53. Kozlovskiy A, Akhmetzhan S, Ivanitskaya N, Kenzhina, Zdorovets M. Study of the effect of irradiation with Ca $^{5+}$ ions on the increase in Ni nanotubes lifetime, applicable as the basis for lithium-ion batteries. Mater Res Express. 2019 May 21;6(8):085074.

54. Mwonga PV, Barik R, Naidoo SR, Quandt A, Ozoemena KI. Interrogating the effects of ion-implantation-induced defects on the energy storage properties of bulk molybdenum disulphide. Phys Chem Chem Phys. 2018;20(44):28232–40.

55. Rahman MM, Chen WY, Mu L, Xu Z, Xiao Z, Li M, et al. Defect and structural evolution under high-energy ion irradiation informs battery materials design for extreme environments. Nat Commun. 2020 Sep 11;11(1):4548.

56. Yao X, Olsson E, Wang M, Wang J, Cai Q, Peng N, et al. Xenon Ion Implantation Induced Surface Compressive Stress for Preventing Dendrite Penetration in Solid-State Electrolytes. Small. 2022 Jun;18(23):2108124.

57. Okamoto NL, Shimokawa K, Tanimura H, Ichitsubo T. Feasible transformation of MgCo2O4 from spinel to defect rocksalt structure under electron irradiation. Scripta Materialia. 2019 Jul 1;167:26–30.

58. Wei B, Lu X, Voisard F, Wei H, Chiu H chieh, Ji Y, et al. In Situ TEM Investigation of Electron Irradiation Induced Metastable States in Lithium-Ion Battery Cathodes: Li2FeSiO4 versus LiFePO4. ACS Appl Energy Mater. 2018 Jul 23;1(7):3180–9.

59. Su D, Wang F, Ma C, Jiang N. Engineering nano-composite Li4Ti5O12 anodes via scanning electron-probe fabrication. Nano Energy. 2013 May 1;2(3):343–50.

60. Lan CK, Chuang SI, Bao Q, Liao YT, Duh JG. One-step argon/nitrogen binary plasma jet irradiation of Li4Ti5O12 for stable high-rate lithium ion battery anodes. Journal of Power Sources. 2015 Feb 1;275:660–7.

61. Cui J, Cao L, Zeng D, Wang X, Li W, Lin Z, et al. Surface Characteristic Effect of Ag/TiO $_2$ Nanoarray Composite Structure on Supercapacitor Electrode Properties. Scanning. 2018 Jul 24;2018:1–10.

62. Le Calvez E, Yarekha D, Fugère L, Robert K, Huvé M, Marinova M, et al. Influence of ion implantation on the charge storage mechanism of vanadium nitride pseudocapacitive thin films. Electrochemistry Communications. 2021 Apr;125:107016.

63. Lee WG, Jang HS, Justin Raj C, Rajesh M, Kim BC, Cho WJ, et al. Effect of proton irradiation on the structural and electrochemical properties of MnO2 nanosheets. Journal of Electroanalytical Chemistry. 2018 Feb 15;811:16–25.

64. Hussain AMP, Kumar A. Enhanced electrochemical stability of all-polymer redox supercapacitors with modified polypyrrole electrodes. Journal of Power Sources. 2006 Oct;161(2):1486–92.

65. Hussain AMP, Saikia D, Singh F, Avasthi DK, Kumar A. Effects of 160MeV Ni12+ ion irradiation on polypyrrole conducting polymer electrode materials for all polymer redox supercapacitor. Nuclear Instruments and Methods in Physics Research Section B: Beam Interactions with Materials and Atoms. 2005 Dec;240(4):834–41.

66. S. Edge J, O'Kane S, Prosser R, D. Kirkaldy N, N. Patel A, Hales A, et al. Lithium ion battery degradation: what you need to know. Physical Chemistry Chemical Physics. 2021;23(14):8200–21.

67. Lu B, Ning C, Shi D, Zhao Y, Zhang J. Review on electrode-level fracture in lithium-ion batteries*. Chinese Phys B. 2020 Feb;29(2):026201.

68. Ding N, Zhu J, Yao YX, Chen CH. The effects of γ-radiation on LiCoO2. Chemical Physics Letters. 2006 Aug 4;426(4):324–8.

69. Saikia D, Kumar A, Singh F, Avasthi DK, Mishra NC. Ionic conduction in 70-MeV C5+-ion-irradiated poly(vinylidenefluoride-co-hexafluoropropylene)-based gel polymer electrolytes. Journal of Applied Physics. 2005 Aug 15;98(4):043514.

70. Kim B, Cho YS, Lee JG, Joo KH, Jung KO, Oh J, et al. Ion-implantation modification of lithium– phosphorus oxynitride thin-films. Journal of Power Sources. 2002 Jun;109(1):214–9.

71. Ahn JH, Eom JY, Kim JH, Kim HW, Lee BC, Kim SS. Synthesis of TiO $_2$ nanoparticles induced by electron beam irradiation and their electrochemical performance as anode materials for Li-ion batteries. Journal of Electrochemical Science and Technology. 2015 Sep 30;6(3):75–80.

72. Liang Y, Lu W. Gamma-irradiation synthesis of Fe3O4/rGO nanocomposites as lithium-ion battery anodes. J Mater Sci: Mater Electron. 2020 Oct 1;31(19):17075–83.

73. Marcano DC, Kosynkin DV, Berlin JM, Sinitskii A, Sun Z, Slesarev A, et al. Improved Synthesis of Graphene Oxide. ACS Nano. 2010 Aug 24;4(8):4806–14.

74. Deghiedy NM, Yousif NM, Hosni HM, Balboul MR. Silver-modified electrodes based on amorphous MnO2/ carbon nanotube: Multicomponent approach to enhance the performance of supercapacitors. Journal of Physics and Chemistry of Solids. 2022 Feb;161:110445.

75. Ma H, Liu J, Hua H, Peng L, Shen X, Wang X, et al. Facile Fabrication of Functionalized Separators for Lithium-Ion Batteries with Ionic Conduction Path Modifications via the γ-Ray Co-irradiation Grafting Process. ACS Appl Mater Interfaces. 2021 Jun 16;13(23):27663–73.

76. Sheng L, Zhang Y, Xie X, Wu H, Yang L, Gao X, et al. Polyethylene separator activated by γ-ray irradiation for improving lithium-based battery performance. J Mater Sci. 2021 Dec;56(36):20026– 36.

77. Aldawsari Y, Mussa Y, Ahmed F, Arsalan M, Alsharaeh E. Novel Synthesis of Holey Reduced Graphene Oxide/Polystyrene (HRGO/PS) Nanocomposites by Microwave Irradiation as Anodes for High-Temperature Lithium-Ion Batteries. Materials. 2019 Jan;12(14):2248.

78. Huang P, Zhang M, Kang J, Feng H, Su Q, Du G, et al. Rapid microwave-irradiation synthesis of ZnCo2O4/ZnO nanocrystals/carbon nanotubes composite as anodes for high-performance lithium-ion battery. J Mater Sci. 2019 Mar 1;54(5):4154–67.

79. Liu Y, Guo B, Zou X, Li Y, Shi S. Machine learning assisted materials design and discovery for rechargeable batteries. Energy Storage Materials. 2020 Oct 1;31:434–50.

80. Wang Q, Zhang G, Li Y, Hong Z, Wang D, Shi S. Application of phase-field method in rechargeable batteries. npj Comput Mater. 2020 Nov 19;6(1):1–8.